

OPTIMUM BOUNDARIES OF SIGNAL-TO-NOISE RATIO FOR ADAPTIVE CODE MODULATIONS

Hyuck M. Kwon, et al.

**Wichita State University
Department of Electrical Engineering and Computer Science
1845 N. Fairmount Ave
Wichita, Kansas 67260-0083**

14 Nov 2017

Final Report

APPROVED FOR PUBLIC RELEASE; DISTRIBUTION IS UNLIMITED.



**AIR FORCE RESEARCH LABORATORY
Space Vehicles Directorate
3550 Aberdeen Ave SE
AIR FORCE MATERIEL COMMAND
KIRTLAND AIR FORCE BASE, NM 87117-5776**

DTIC COPY

NOTICE AND SIGNATURE PAGE

Using Government drawings, specifications, or other data included in this document for any purpose other than Government procurement does not in any way obligate the U.S. Government. The fact that the Government formulated or supplied the drawings, specifications, or other data does not license the holder or any other person or corporation; or convey any rights or permission to manufacture, use, or sell any patented invention that may relate to them.

This report is the result of contracted fundamental research which is exempt from public affairs security and policy review in accordance with AFI 61-201, paragraph 2.3.5.1. This report is available to the general public, including foreign nationals. Copies may be obtained from the Defense Technical Information Center (DTIC) (<http://www.dtic.mil>).

AFRL-RV-PS-TR-2017-0124 HAS BEEN REVIEWED AND IS APPROVED FOR
PUBLICATION IN ACCORDANCE WITH ASSIGNED DISTRIBUTION STATEMENT.

//SIGNED//

KHANH PHAM
Program Manager

//SIGNED//

DAVID CARDIMONA
Technical Advisor, Space Based Advanced Sensing
and Protection

//SIGNED//

JOHN BEAUCHEMIN
Chief Engineer, Spacecraft Technology Division
Space Vehicles Directorate

This report is published in the interest of scientific and technical information exchange, and its publication does not constitute the Government's approval or disapproval of its ideas or findings.

Approved for public release; distribution is unlimited.

| REPORT DOCUMENTATION PAGE | | | | Form Approved OMB No. 0704-0188 | |
|---|--------------|--------------------------------|----------------------------|---|---|
| Public reporting burden for this collection of information is estimated to average 1 hour per response, including the time for reviewing instructions, searching existing data sources, gathering and maintaining the data needed, and completing and reviewing this collection of information. Send comments regarding this burden estimate or any other aspect of this collection of information, including suggestions for reducing this burden to Department of Defense, Washington Headquarters Services, Directorate for Information Operations and Reports (0704-0188), 1215 Jefferson Davis Highway, Suite 1204, Arlington, VA 22202-4302. Respondents should be aware that notwithstanding any other provision of law, no person shall be subject to any penalty for failing to comply with a collection of information if it does not display a currently valid OMB control number. PLEASE DO NOT RETURN YOUR FORM TO THE ABOVE ADDRESS. | | | | | |
| 1. REPORT DATE (DD-MM-YY) 14-11-2017 | | 2. REPORT TYPE Final Report | | 3. DATES COVERED (From - To) 6 Jan 2016 – 6 Sep 2017 | |
| 4. TITLE AND SUBTITLE Optimum Boundaries of Signal-to-Noise Ratio for Adaptive Code Modulations | | | | 5a. CONTRACT NUMBER FA9453-16-1-0049 | |
| | | | | 5b. GRANT NUMBER | |
| | | | | 5c. PROGRAM ELEMENT NUMBER 62601F | |
| 6. AUTHOR(S) Hyuck M. Kwon, Krittetash Pinyoanuntapong, and Shuang Feng | | | | 5d. PROJECT NUMBER 8809 | |
| | | | | 5e. TASK NUMBER PPM00004291 | |
| | | | | 5f. WORK UNIT NUMBER EF127218 | |
| 7. PERFORMING ORGANIZATION NAME(S) AND ADDRESS(ES) Wichita State University Department of Electrical Engineering and Computer Science 1845 N. Fairmount Ave Wichita, Kansas 67260-0083 | | | | 8. PERFORMING ORGANIZATION REPORT NUMBER R51448 | |
| 9. SPONSORING / MONITORING AGENCY NAME(S) AND ADDRESS(ES) Air Force Research Laboratory Space Vehicles Directorate 3550 Aberdeen Ave., SE Kirtland AFB, NM 87117-5776 | | | | 10. SPONSOR/MONITOR'S ACRONYM(S) AFRL/RVSW | |
| | | | | 11. SPONSOR/MONITOR'S REPORT NUMBER(S) AFRL-RV-PS-TR-2017-0124 | |
| 12. DISTRIBUTION / AVAILABILITY STATEMENT Approved for public release; distribution is unlimited. | | | | | |
| 13. SUPPLEMENTARY NOTES | | | | | |
| 14. ABSTRACT This report studies how to decide the boundaries of a signal-to-noise ratio for the adaptive code modulation mode selection, for a given set of parameters and system model. Also, this report proposes an efficient and practical algorithm to search the proper adaptive code modulation mode that meets a target bit error rate and achieves the maximum data rate. The proposed algorithm is found to be effective under jamming and interference, even if channel and jamming state information are unavailable. This report also discusses experimental setups and test results using Universal Software Radio Peripheral hardware radio communications systems. | | | | | |
| 15. SUBJECT TERMS Adaptive code modulation, jamming, satellite communications, Rician fading, convolutional code, low density parity check code | | | | | |
| 16. SECURITY CLASSIFICATION OF: | | | 17. LIMITATION OF ABSTRACT | 18. NUMBER OF PAGES | 19a. NAME OF RESPONSIBLE PERSON |
| a. REPORT | b. ABSTRACT | c. THIS PAGE | | | 19b. TELEPHONE NUMBER (include area code) |
| Unclassified | Unclassified | Unclassified | Unlimited | 76 | Khanh Pham |

(This page intentionally left blank)

Table of Contents

| | |
|--|----|
| 1. Summary..... | 1 |
| 2. Introduction..... | 2 |
| 3. Assumptions (System Model)..... | 3 |
| 4. Procedure (How To Select Adaptive Code Modulation)..... | 7 |
| 5. Result and Discussions..... | 15 |
| 6. Conclusions..... | 25 |
| References..... | 26 |
| Appendix A: USRP Front Panel Block Diagrams..... | 29 |
| Appendix B: USRP Back Panel Block Diagrams..... | 44 |
| List of Acronyms and Abbreviations..... | 66 |

List of Figures

| | |
|--|----|
| Fig. 1. System Model..... | 3 |
| Fig. 2. Plots of bit error rate $P_b(\gamma)$ versus $g=E_b/N_0$ in dB under AWGN for ten ACM modes, assuming no jamming and jamming with E_b/N_J . Crossing points at $P_b = 10^{-3}$ are marked by triangles in red and blue for no jamming and jamming, respectively..... | 9 |
| Fig. 3. Flow chart of proposed ACM mode selection when JSI is unavailable..... | 12 |
| Fig. 4. Instantaneous spectral efficiency versus $g = E_b/N_0$ in dB for no jamming (Case A), jamming with JSI (Case B), and jamming without JSI (Case C). No fading is considered..... | 16 |
| Fig. 5. Average bandwidth efficiency comparisons of Cases A, B, and C. Average is taken over Rician fading of Rician factor $K = 5$ | 17 |
| Fig. 6. Average BER comparisons of Cases A, B, and C. Average is taken over Rician fading of Rician factor $K = 5$ | 18 |
| Fig. 7. Comparison of \bar{g} and \bar{g}_J | 19 |
| Fig. 8. Plots of bit error rate $P_b(g)$ versus $g = E_b/N_0$ in dB for 20 ACM modes applied FEC LDPC coding under AWGN, assuming no jamming. Crossing points at $P_b(g) = 10^{-5}$ are marked by triangles in red. | 20 |
| Fig. 9. Instantaneous spectral efficiency versus $g = E_b/N_0$ in dB applied FEC LDPC from Table 3, for no jamming (Case A), jamming with JSI (Case B), and jamming without JSI (Case C). No fading is considered..... | 21 |
| Fig. 10. Average bandwidth efficiency comparisons of Cases A, B, and C applied FEC LDPC from Table 3. Average is taken over Rician fading of Rician factor $K = 5$ | 21 |
| Fig. 11. Average bandwidth efficiency comparisons of Cases A, B, and C versus PBTJ fraction b . Average is taken over Rician fading of Rician factor $K = 0.1$ with $E_b/N_J = 5$ dB, E_b/N_0 target = 10 dB and BER target = 10^{-3} | 22 |
| Fig. 12. Average bandwidth efficiency comparisons of Cases A, B, and C versus PBTJ fraction β . Average is taken over Rician fading of Rician factor $K = 5$ with $E_b/N_J = 20$ dB, E_b/N_0 target = 10 dB and BER target = 10^{-3} | 23 |

List of Tables

| | |
|--|----|
| Table 1. Generator matrices for convolutional code of constraint length 7 and code rates 1/2, 1/3, 1/4, and 2/3..... | 4 |
| Table 2. SNR boundaries for ten ACM modes under AWGN or AWGN plus jamming with $E_b/N_j = 10$ dB and $\beta = 1$ | 4 |
| Table 3. SNR boundaries for 20 ACM modes applied FEC LDPC coding under AWGN or AWGN plus jamming..... | 5 |
| Table 4. Process of proposed algorithm using input SNR $\gamma_{b,1} = 1.5$ dB | 13 |
| Table 5. Selected ACM modes for Case C using AWGN SNR. Boundaries under AWGN plus jamming with $E_b/N_j = 10$ dB and $\beta = 1$ | 14 |

ACKNOWLEDGMENTS

This material is based on research sponsored by the Air Force Research Laboratory under agreement number FA9453-16-1-0049. The U.S. Government is authorized to reproduce and distribute reprints for Governmental purposes notwithstanding any copyright notation thereon.

DISCLAIMER

The views and conclusions contained herein are those of the authors and should not be interpreted as necessarily representing the official policies or endorsements, either expressed or implied, of the Air Force Research Laboratory or the U.S. Government.

1. Summary

This report achieved the three objectives stated in the original proposal during the period from January 6, 2016, to July 5, 2017, by doing the following:

- Investigated the optimal decision boundaries of the received signal-to-noise ratio (SNR) for an optimal adaptive code modulation (ACM) selection out of multiple available candidates to maximize the bandwidth efficiency.
- Proved the proposed concept through simulation.
- Evaluated the merits and disadvantages of the proposed strategy by doing the following: (1) comparing the bit error rate (BER) and bandwidth efficiency performance in bits per second per hertz of the proposed ACM scheme with those of the existing non-adaptive schemes in the presence of partial-band noise jamming (PBNJ), (2) computing the computational complexities, and (3) addressing feasibility and compatibility of the proposed scheme with existing schemes.
- In addition, performed experimental tests using Universal Software Radio Peripheral (USRP) hard- ware radio communications systems, and confirmed that jamming signal can degrade performance significantly.

These achievements are summarized in this final report, and the contents were disclosed in part through a peer-reviewed conference proceeding publication: Krtittetash Pinyoanuntapong, Madhuprana Goswami, Ashfia Binte Habib, Hyuck M. Kwon, and Khanh Pham, Boundaries of Signal-to-Noise Ratio for Adaptive Code Modulations, IEEE Military Communications Conf., Baltimore, MD, November 13, 2016.

2. Introduction

Adaptive code modulation (ACM) has been studied to enhance the bandwidth and power efficiency in a bandwidth- and power-constrained communication system environment [1]–[3]. For example, the authors in [1] examined the integration of adaptive modulation and channel coding protocols with fountain coding in a packet radio system. Also, the existing digital video broadcasting-return channel via satellite (DVB-RCS) and the second-generation digital video broadcasting satellite (DVB-S2) including the future protected tactical waveform have employed an ACM [4]–[9].

This report studies how to determine the ACM boundaries of the SNR for a given set of parameters and the system model. The results here will be useful for future satellite communication system designs under jamming and interference environments.

This report is organized as follows: Section II describes the system model, and Section III presents how to select the ACM out of a pool, assuming that jamming and interference state information is both available and unavailable at the receiver. Section IV compares and discusses the numerical results for three cases, and Section V concludes the report.

Appendices A and B describe and teach, respectively, the front and back panel block diagrams of a Universal Software Radio Peripheral (USRP) 2932 used for testing the concepts in the research project with hardware radio communications systems.

3. Assumptions (System Model)

Fig. 1 represents the overall system block diagram.

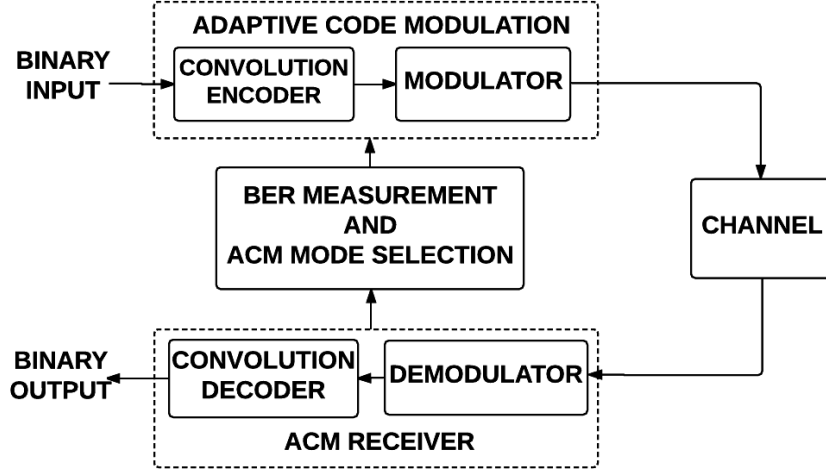


Fig. 1: System model.

3.1 Adaptive Code Modulation Model

Two sets of adaptive code modulations are considered here. The first set is composed of ten modes, which are combinations of two M-ary phase shift keying (MPSK) modulations (i.e., quadrature phase shift keying (QPSK) and 8-ary phase shift keying (8PSK) and a convolutional forward error correction (FEC) code of five different code rates (i.e., convolutional code of 1/4, 1/3, 1/2, 2/3, and 1). The connection generator matrices for a convolutional code of constraint length 7 for these code rates are listed in Table 1 [10]. The code rates and the constraint length are obtained from the DVB-S2 standard [9]. The ten ACM modes are listed in Table 2. The second ACM set is composed of 20 modes, which are combinations of two modulations, QPSK and 8PSK, and a low-density parity-check (LDPC) FEC code of 12 code rates (i.e., 1/4, 1/3, 2/5, 1/2, 3/5, 2/3, 3/4, 4/5, 5/6, 8/9, 9/10, and 1). For QPSK, all 12 code rates are used, whereas for 8PSK, only eight code rates are used: 3/5, 2/3, 3/4, 4/5, 5/6, 8/9, 9/10, and 1. This is because the bandwidth efficiency of 8PSK with a low code rate (1/4, 1/3, 2/5, 1/2) is lower than that of QPSK with a 9/10 rate. These code rates are obtained from DVB-S2 standard [9, p. 13]. The twenty ACM modes are listed in Table 3.

Table 1: Generator matrices for convolutional code of constraint length 7 and code rates 1/2, 1/3, 1/4, and 2/3.

| Code Rate | Generator Matrix (Constraint Length 7) | d_{free} | Coding Gain (dB) $G_c \approx d_{free} R_c$ |
|-----------|---|------------|--|
| 1 | 0 | No coding | 0 |
| 1/4 | [163 147 135 135] | 22 | 7.4 |
| 1/3 | [171 165 133] | 15 | 7 |
| 1/2 | [155 177] | 8 | 6 |
| 2/3 | $\begin{bmatrix} 5 & 23 & 27 \\ 17 & 15 & 13 \end{bmatrix}$ | 5 | 5.22 |

Table 2: SNR boundaries for ten ACM modes under AWGN or AWGN plus jamming with $E_b / N_J = 10 \text{ dB}$ and $b = 1$.

| i | ACM Mode | Bandwidth Efficiency $\frac{R(\gamma_{b,i})}{B} = (\log_2 M) R_c$ (bits / (s · Hz)) | SNR Lower bound $\gamma_{b,i}$ in dB for ACM mode i | |
|-----|-------------------------------|---|--|--|
| | | | No Jamming | Under Jamming |
| 0 | No transmission | 0 | - | - |
| 1 | QPSK + R_c 1/4 | 0.5 | $\gamma_{b,1} = 1.3$ | $\gamma_{b,1,J} = 1.9$ |
| 2 | QPSK + R_c 1/3 | 0.66 | $\gamma_{b,2} = 2.0$ | $\gamma_{b,2,J} = 2.7$ |
| 3 | QPSK + R_c 1/2 | 1 | $\gamma_{b,3} = 2.2$ | $\gamma_{b,3,J} = 3.0$ |
| 4 | QPSK + R_c 2/3 | 1.33 | $\gamma_{b,4} = 3.6$ | $\gamma_{b,4,J} = 4.8$ |
| 5 | 8PSK + R_c 1/4 | 0.75 | $\gamma_{b,5} = 4.6$ | $\gamma_{b,5,J} = 6.1$ |
| 6 | 8PSK + R_c 1/3 | 1 | $\gamma_{b,6} = 5.3$ | $\gamma_{b,6,J} = 7.2$ |
| 7 | 8PSK + R_c 1/2 | 1.5 | $\gamma_{b,7} = 5.6$ | $\gamma_{b,7,J} = 7.5$ |
| 8 | QPSK + R_c 1 (No coding) | 2 | $\gamma_{b,8} = 6.8$ | $\gamma_{b,8,J} = 9.6$ |
| 9 | 8PSK + R_c 2/3 | 2 | $\gamma_{b,9} = 7.0$ | $\gamma_{b,9,J} = 10.0$ |
| 10 | 8PSK + R_c 1 (No coding) | 3 | $\gamma_{b,10} = 10.0$ | $\gamma_{b,10,J} = \infty$ cannot be achieved |

Column 1 is ACM mode index (i), and ACM mode has BER target, $P_b(\gamma_{b,i}) = 10^{-3}$, where $\gamma_{b,i} \leq \gamma < \gamma_{b,i+1}$.

3.2 Channel Model

A Rician fading channel in addition to additive white Gaussian noise channel (AWGN) is considered instead of Rayleigh fading because the line-of-sight (LOS) component is typically available in a satellite communication system.

Table 3: SNR boundaries for 20 ACM modes applied FEC LDPC coding under AWGN or AWGN plus jamming.

| i | ACM Mode | Bandwidth Efficiency (bps/Hz) | SNR Lower Bound $\gamma_{b,i}$ in dB for ACM Mode i | |
|-----|-------------------|------------------------------------|--|----------------------------|
| | | | No Jamming | Under Jamming |
| 0 | No transmission | 0 | - | - |
| 1 | QPSK + $R_c 1/4$ | 0.5 | $\gamma_{b,1} = -2.8$ | $\gamma_{b,1,J} = -2.57$ |
| 2 | QPSK + $R_c 1/3$ | 0.66 | $\gamma_{b,2} = -1.5$ | $\gamma_{b,2,J} = -1.18$ |
| 3 | QPSK + $R_c 2/5$ | 0.8 | $\gamma_{b,3} = -0.59$ | $\gamma_{b,3,J} = -0.19$ |
| 4 | QPSK + $R_c 1/2$ | 1 | $\gamma_{b,4} = 0.85$ | $\gamma_{b,4,J} = 1.41$ |
| 5 | QPSK + $R_c 3/5$ | 1.2 | $\gamma_{b,5} = 2.1$ | $\gamma_{b,5,J} = 2.87$ |
| 6 | QPSK + $R_c 2/3$ | 1.33 | $\gamma_{b,6} = 3.0$ | $\gamma_{b,6,J} = 3.97$ |
| 7 | QPSK + $R_c 3/4$ | 1.5 | $\gamma_{b,7} = 3.9$ | $\gamma_{b,7,J} = 5.12$ |
| 8 | QPSK + $R_c 4/5$ | 1.6 | $\gamma_{b,8} = 4.5$ | $\gamma_{b,8,J} = 5.94$ |
| 9 | QPSK + $R_c 5/6$ | 1.66 | $\gamma_{b,9} = 5.0$ | $\gamma_{b,9,J} = 6.65$ |
| 10 | QPSK + $R_c 8/9$ | 1.77 | $\gamma_{b,10} = 6.1$ | $\gamma_{b,10,J} = 8.37$ |
| 11 | QPSK + $R_c 9/10$ | 1.8 | $\gamma_{b,11} = 6.3$ | $\gamma_{b,11,J} = 8.72$ |
| 12 | QPSK no coding | 2 | $\gamma_{b,12} = 9.6$ | $\gamma_{b,12,J} = 20$ |
| 13 | 8PSK + $R_c 3/5$ | 1.8 | $\gamma_{b,13} = 5.38$ | $\gamma_{b,13,J} = 7.22$ |
| 14 | 8PSK + $R_c 2/3$ | 2 | $\gamma_{b,14} = 6.43$ | $\gamma_{b,14,J} = 8.94$ |
| 15 | 8PSK + $R_c 3/4$ | 2.25 | $\gamma_{b,15} = 7.72$ | $\gamma_{b,15,J} = 11.61$ |
| 16 | 8PSK + $R_c 4/5$ | 2.4 | $\gamma_{b,16} = 8.61$ | $\gamma_{b,16,J} = 14.23$ |
| 17 | 8PSK + $R_c 5/6$ | 2.5 | $\gamma_{b,17} = 9.2$ | $\gamma_{b,17,J} = 16.95$ |
| 18 | 8PSK + $R_c 8/9$ | 2.66 | $\gamma_{b,18} = 10.51$ | $\gamma_{b,18,J} = 19.48$ |
| 19 | 8PSK + $R_c 9/10$ | 2.7 | $\gamma_{b,19} = 10.82$ | $\gamma_{b,19,J} = 17.64$ |
| 20 | 8PSK no coding | 3 | $\gamma_{b,20} = 13$ | $\gamma_{b,20,J} = \infty$ |

*Jamming with $E_b / N_j = 10$ dB and $\beta = 1$. BW efficiency is computed by $R(\gamma_{b,i})/B|_{B=1} = (\log_2 M) R_c$. Column 1 is ACM mode index (i), and ACM mode has BER target, $P_b(\gamma_{b,i}) = 10^{-5}$, where $\gamma_{b,i} \leq \gamma < \gamma_{b,i+1}$.

This report assumes PBNJ. Interference can be added with no difficulty because this report considers an AWGN type of interference. The proposed algorithm is effective for any other type of interference and jamming because the proposed algorithm uses BER criteria to select the ACM mode and does not have the jamming and interference state information. Therefore, this report

assumes a PBNJ without loss of generality. The probability of being jammed (denoted by β) is between 0 and 1. The probability density function of the instantaneous received symbol SNR in a Rician fading channel is written as

$$p_\gamma(\gamma) = \frac{K+1}{\bar{\gamma}} \exp\left[-K - \frac{(K+1)\gamma}{\bar{\gamma}}\right] I_0\left[2\sqrt{\frac{K(K+1)\gamma}{\bar{\gamma}}}\right] \quad (1)$$

where $\bar{\gamma} = E[\gamma]$ is the expectation of an instantaneous SNR $\gamma = |h|^2 E_s/N_0$ or $\gamma = |h|^2 E_s/(N_0 + \beta N_J)$ under Rician fading, depending on the jamming state, K is the Rician fading factor and $|h|^2$ is the Rician fading coefficient whose average power is written from [3], pages 78-79, as

$$E[|h|^2] = 2\sigma^2(K+1) \quad (2)$$

where, $E_s/N_0 = (\log_2 M) E_b/N_0$ and $E_s/(N_J + N_0) = (\log_2 M) \cdot E_b/(N_J + N_0)$ are symbol energy-to-noise power spectral density ratio and symbol energy-to-jamming-plus-noise power spectral density ratio, respectively, where E_b is the bit energy, and M is 4 or 8.

The probability that the selected ACM mode information is fed back to the transmitter incorrectly is negligible. This is because the amount of feedback information is very small, compared to the amount of data, and sufficient power can be allocated for the ACM mode information transmission. The transmitter applies the received ACM mode information for the next frame interval. Each frame (or an update time interval for ACM) consists of a sufficient number of data bits to estimate BER (or packet error probability) reliably. For example, 100,000 bits per frame is sufficient for a target BER of 10^{-3} .

The average of the received symbol SNR can be written as

$$\text{Avg. SNR} = \begin{cases} \bar{\gamma} = E[|h|^2] \frac{E_s}{N_0} & \text{no jamming} \\ \bar{\gamma}_J = E[|h|^2] \left(\frac{\frac{E_s}{\beta N_J} \frac{E_s}{N_0}}{\frac{E_s}{\beta N_J} + \frac{E_s}{N_0}} \right) & \text{jamming} \\ & \text{w/ prob. } \beta. \end{cases} \quad (3)$$

4. Procedure (How To Select Adaptive Code Modulation)

This section presents a method for how to select an ACM mode out of ten possible combinations of convolutional FEC and QPSK/8PSK modulations (or twenty combinations of LDPC FEC and QPSK/8PSK modulation) when the instantaneous SNR is time-varying due to the presence of fading and jamming/interference. Case A in this section finds lower and upper SNR boundaries, i.e., SNR region for each ACM mode to be used, assuming an AWGN channel of E_s / N_0 . Case B assumes that jamming state information (JSI) (e.g., E_s / N_J and jamming probability β) is available at the receiver and finds the SNR region for each ACM mode using the known JSI. Case C assumes that JSI is unknown at the receiver and presents an efficient algorithm for how to select a proper ACM mode based on a BER or symbol error rate test using the SNR regions obtained for Case A.

4.1 SNR Boundaries under AWGN

SNR boundaries will be determined to guarantee that the instantaneous BER under fading is less than or equal to the maximum allowable BER. For example, the maximum BER is set to $P_{b,\max} = 10^{-3}$ for combinations of convolutional FEC and QPSK/8PSK, and $P_{b,\max} = 10^{-5}$ for combinations of LDPC FEC and QPSK/8PSK modulations in this report; hence, the instantaneous BER $P_b(g) \leq P_{b,\max} = 10^{-3}$ or 10^{-5} . If an MPSK and a convolutional error correction code are employed, then an explicit union upper bound of the BER after the convolution decoding can be written from [11], as

$$P_b(\gamma) \leq \sum_{d=d_{\text{free}}}^{\infty} a(d) P_d(\gamma) \quad (4)$$

for a given instantaneous symbol SNR $g = (\log_2 M)g_b$, where g_b is the instantaneous bit SNR, d is the Hamming distance between the correct convolutional code word trellis path and an incorrect trellis path, $a(d)$ is the number of incorrect paths whose distance from the correct path is $d \geq d_{\text{free}}$, which is uncorrectable, and $P_d(\gamma)$ is the pairwise convolutional error correction code word error probability due to decoding the received word incorrectly from the correct code word trellis path to an incorrect code word trellis path of distance d . Here, $P_d(\gamma)$ can be written

as

$$P_d(\gamma) \approx Q\left(\sqrt{2dR_c\gamma} \sin \pi/M\right) = Q\left(\sqrt{2dR_c(\log_2 M)\gamma_b} \sin \pi/M\right) \quad (5)$$

where $Q(\alpha) = \int_{\alpha}^{\infty} 1/\sqrt{2\pi} \exp(-t^2/2) dt$ is the tail probability of a normalized Gaussian random

variable larger than or equal to α , R_c is the code rate, and it is assumed that whenever a code symbol error occurs, it is demodulated into a wrong symbol with the minimum distance in the MPSK signal constellation. Fig. 2 shows BER versus $g_b = E_b/N_0 = (E_s/N_0)/\log_2 M$ for the ten ACM modes under AWGN, using (4) and (5). The crossing points at $P_b = 10^{-3}$ marked by red triangles are the lower boundaries of $g_{b,i}$ for ACM mode i under the AWGN when there is no jamming.

Table 2 lists the SNR boundaries for the no-jamming case using the results in Fig. 2. Note that the bandwidth efficiencies under 8PSK with code rates 1/4 and 1/3 are lower than that of QPSK with code rate 2/3, but they require a higher SNR in order to maintain 10^{-3} BER. Thus, the 8PSK modulation with code rates 1/4 and 1/3 are neglected. Under a fading environment, the SNR will vary. If it is known at the receiver, then the proper ACM mode can be selected using the SNR boundaries from Table 2.

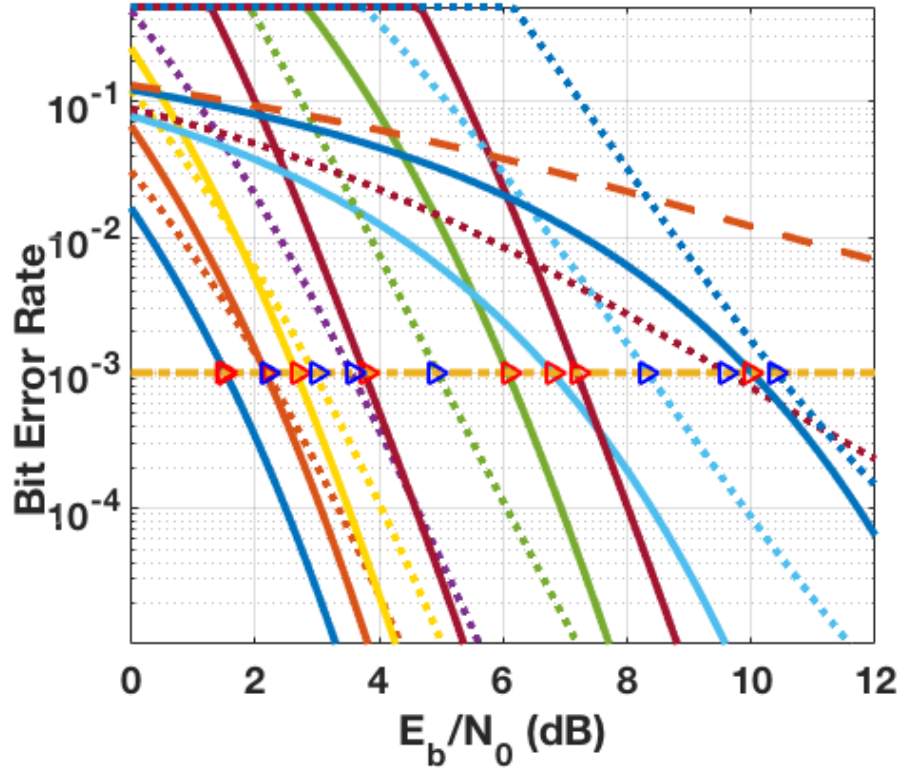


Fig. 2: Plots of bit error rate $P_b(\gamma)$ versus $g = E_b/N_0$ in dB under AWGN for ten ACM modes, assuming no jamming and jamming with E_b/N_J . Crossing points at $P_b = 10^{-3}$ are marked by triangles in red and blue for no jamming and jamming, respectively.

4.2 SNR Boundaries under Jamming with JSI

When the transmitted signal is jammed with $E_b/N_J = 10$ dB and jamming probability $\beta = 1$, for example, the required crossing boundary point $\gamma_{b,i,J}$ for the ACM mode to achieve the same $P_b(\gamma) = 10^{-3}$ is shifted to a higher SNR than $\gamma_{b,i}$ because the effective symbol energy-to-jamming-plus-noise ratio (SJNR) is $\gamma = |h|^2 E_s / (N_0 + N_J / \beta)$ under AWGN and jamming (but no fading).

This SJNR can be rewritten as

$$SJNR = \frac{E_s}{N_J / \beta} \frac{E_s}{N_0} \bigg/ \left(\frac{E_s}{N_J / \beta} + \frac{E_s}{N_0} \right) \quad (6)$$

It is interesting to know the shifting amount $(10\log_{10} \mathcal{G}_{b,i,J}) - (10\log_{10} \mathcal{G}_{b,i})$ in dB for the transmitter to use the same ACM mode under jamming with known JSI. This amount indicates how much the transmitter needs to increase its transmitter power P_T or SNR E_s/N_0 in (6) because $E_s = PT$ and the one-side AWGN power spectral density level N_0 and symbol time T are constant. If the transmitter cannot change its transmit power, then this shifting amount indicates selecting a proper ACM mode to achieve the same target BER. This report assumes a constant transmit power, i.e., no power adaptation but rate adaptation because typical satellite systems use constant power.

In Fig. 2 the crossing points at $P_b(\gamma) = 10^{-3}$ are marked by triangles in blue color, and they are the lower SNR boundaries for ACM mode i under jamming. Note that the horizontal axis in Fig. 2 is not SJNR but SNR $\gamma_b = E_b/N_0$. The symbol SNR boundary $\gamma_{i,J} = E_s/N_0$ under jamming can be expressed in terms of known JSI $(E_s/N_J, \beta)$ and SNR boundary $\gamma_i = E_s/N_0$ obtained under no jamming from $P_b(\gamma_i) = P_b(SJNR(\gamma_{i,J})) = 10^{-3}$ as

$$\gamma_{i,J} = \frac{E_s}{\beta N_J} \gamma_i \bigg/ \left(\frac{E_s}{\beta N_J} - \gamma_i \right) \quad (7)$$

This is obtained from (6) by setting

$$\gamma_i = SJNR(\gamma_{i,J}) = \frac{E_s}{\beta N_J} \gamma_{i,J} \bigg/ \left(\frac{E_s}{\beta N_J} + \gamma_{i,J} \right) \quad (8)$$

And this is because both BERs are approximately a function of the tail probability $Q(\alpha)$ for both Cases A and B.

Again, the SJNR \mathcal{G}_J will vary under a fading environment. If \mathcal{G}_J is known at the receiver, i.e., channel state information $(E_s/N_0, E_s/N_J, \beta)$ are known, then the proper ACM mode can be selected using Table 2 for the jamming case because Table 2 lists the SNR boundaries $\mathcal{G}_{b,i,J}$ at the fifth column for the jamming case, using the blue marks in Fig. 2. Note also that 8PSK with no coding cannot be used because $P_b(\gamma) = 10^{-3}$ cannot be achieved, even at $\mathcal{G}_{b,10,J} = \infty$. Note that

the gap between $\mathcal{G}_{i,J}$ and \mathcal{G}_i in dB, i.e., $(10\log_{10} \mathcal{G}_{b,i,J}) - (10\log_{10} \mathcal{G}_{b,i})$ in dB, by using (7), matches closely with the gap between $\mathcal{G}_{b,i,J}$ and $\mathcal{G}_{b,J}$ in dB in Table 2. Furthermore, from (7), a simple theorem can be stated.

Theorem 1: The ACM mode i can be used only if $E_s/N_J/b^3 \geq \mathcal{G}_i$. Else, the ACM mode i cannot be employed.

Proof of Theorem 1: This is because the denominator in (7) becomes negative.

For example, ACM mode $i = 10$ in Table 2 cannot be employed when $E_b/N_J = 10$ dB and $b = 1$.

4.3 SNR Boundaries under Jamming without JSI

If the channel is jammed but JSI is unknown, then a proper ACM mode cannot be selected directly from the fifth column of Table 2 because \mathcal{G}_J is unavailable, i.e., E_b/N_J and b are unknown. Therefore, we propose to use the boundaries \mathcal{G}_i obtained for Case A (unjammed case) and employ the BER criteria of whether a trial ACM mode satisfies $P_b(\gamma_J) \leq 10^{-3}$ or not. When the trial ACM mode satisfies the required BER during the current test interval (which is less than the channel coherence time that can be a frame of multiple symbols), then move the trial ACM mode to the next ACM mode of a higher bandwidth efficiency for the next test transmission. If the chosen ACM mode still satisfies the BER requirement, then move to the next ACM mode again. If the new trial ACM mode does not satisfy the BER requirement, then move down the ACM mode, and so on.

Fig. 3 shows the flow chart of the proposed algorithm in detail. Since only the boundaries \mathcal{G}_i obtained for Case A (unjammed case) are available, the algorithm will find which ACM mode is appropriate to use boundary \mathcal{G}_i for Case C with unknown received SJNR \mathcal{G}_J by using the simple BER test.

In Fig. 3, the algorithm uses the bisection search method, which has the starting point at the middle of available ACM modes. L_max and L_min are the highest and lowest ACM mode available, respectively, e.g., mode 8 and 0 in Table 2. Variable g is the chosen ACM mode index

computed by $(L_max + L_min)/2$. The following explanation is presented to demonstrate the process of the proposed algorithm using the example in Table 4. The flow chart starts at the first input cutoff SNR, $g_{b,1} = 1.5 \text{ dB}$. The initial L_max and L_min are 8 and 0, according to Table 2. The receiver sets the counting index to $g = (L_max + L_min)/2 = 4$ and initializes it using the ACM mode 4, which is QPSK modulation with a code rate 2/3, even under a jamming environment, because the receiver has no JSI. At this modulation, the receiver can achieve the target BER 10^{-3} (refer to the broken red line in Fig. 2 and column 5 of Table 2). The L_max is reassigned to 4, and the index g is now equal to $(4+0)/2=2$ and using mode 2, which is QPSK

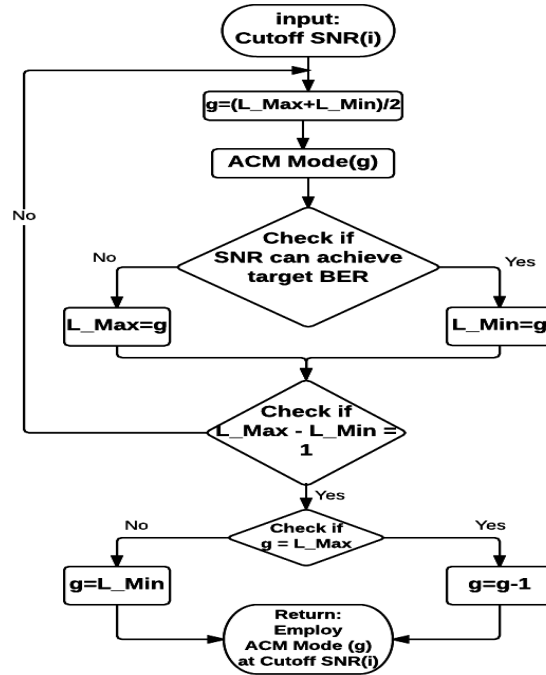


Fig. 3: Flow chart of proposed ACM mode selection when JSI is unavailable.

modulation with a code rate 1/3. The receiver detects that the BER target is satisfied and continues checking until $L_max = 1$. At this modulation, the receiver cannot achieve 10^{-3} BER because of the jamming signal presence, e.g., $E_b/N_j = 10 \text{ dB}$. Refer to the broken red line in Fig. 2 and column 5 of Table 2. This needs to be at least 2.2 dB to achieve the target BER 10^{-3} . The receiver lowers the trial ACM index (i.e., $g = g - 1$), which becomes 0 ACM mode, i.e., no transmission

for the first boundary, i.e., g_1 . Hence, the algorithm outputs no transmission ACM mode for region 1, i.e., $g_1 \leq g_J < g_2$. This process continues until the last boundary, e.g., g_8 , is decided. Therefore, the proposed algorithm can indicate what ACM mode should be used, even if the jamming state information is not available.

Table 4: Process of proposed algorithm using input SNR $g_{b,1} = 1.5 \text{ dB}$.

| L_MAX | L_MIN | $g = (L_Max + L_Min)/2$ | Mode(g) $P_b \leq 10^{-3}$ |
|--------------|--------------|---------------------------|--------------------------------------|
| 8 | 0 | 4 | Yes |
| 4 | 0 | 2 | Yes |
| 2 | 0 | 1 | Yes |
| 1 | 0 | 0 | No |

Input SNR $g_{b,1} = 1.5 \text{ dB}$. Number of possible ACM modes = 8.

Another advantage of this mode-search is that the maximum trial frame test in each loop is equal to half of the number of possible ACM modes. This will decrease the searching time by half when compared to the mode search using a linear searching (sequential) method.

The decision based on boundaries is made for calculating the bandwidth efficiency and data rate. In practice, the algorithm presented in Fig. 3 can accept an instantaneous SNR g and select the proper ACM modulation based on the given γ to maximize the bandwidth efficiency and data rate.

Table 5 lists the selected ACM mode based on the SNR $g_{b,i,J}$ boundaries from Case A. The ACM modes listed in column 2 of Table 5 are selected based on the proposed algorithm to achieve the target BER 10^{-3} under the presence of the jamming signal with $E_b/N_J = 10 \text{ dB}$ and jamming probability $b = 1$.

The average bandwidth efficiency is computed as

$$\bar{R}(\gamma)/B \Big|_{B=1} = \sum_{i=1}^{N_{\text{mode}}} R(\gamma_i)/B \cdot \Pr(\text{mode } i \text{ is selected}) \Big|_{B=1}, \quad (9)$$

$$\Pr(\text{mode } i \text{ is selected}) = \int_{\gamma_i}^{\gamma_{i+1}} p_\gamma(\gamma) d\gamma, \quad (10)$$

where N_{mode} is the number of possible ACM modes, B is the channel bandwidth equal to the inverse

of the symbol interval $1/T$ and normalized to 1, and $p_\gamma(\gamma)$ is the probability density function of Rician fading in (1) with Rician factor K and the average received SNR $\bar{\gamma}$.

Table 5: Selected ACM modes for Case C using AWGN SNR. Boundaries under AWGN plus jamming with $E_b/N_J = 10$ dB and $b = 1$.

| i | Selected ACM Mode | Bandwidth Efficiency | SNR Lower Bound $\gamma_{b,i}$ |
|-----|-------------------|---|---------------------------------------|
| | | $\frac{R(\gamma_{b,i})}{B} = (\log_2 M) R_c$ (bits / (s · Hz)) | in dB for ACM Mode i Without JSI |
| 0 | No transmission | 0 | - |
| 1 | No transmission | 0 | $\gamma_{b,1} = 1.5$ |
| 2 | QPSK + R_c 1/4 | 0.5 | $\gamma_{b,2} = 2.2$ |
| 3 | QPSK + R_c 1/4 | 0.5 | $\gamma_{b,3} = 2.7$ |
| 4 | QPSK + R_c 1/2 | 1 | $\gamma_{b,4} = 3.8$ |
| 5 | QPSK + R_c 2/3 | 1.33 | $\gamma_{b,5} = 6.1$ |
| 6 | QPSK + R_c 2/3 | 1.33 | $\gamma_{b,6} = 6.8$ |
| 7 | QPSK + R_c 2/3 | 1.33 | $\gamma_{b,7} = 7.0$ |
| 8 | 8PSK + R_c 2/3 | 2 | $\gamma_{b,8} = 10.0$ |

Column 1 is ACM mode index (i), and ACM mode has BER target $P_b(\gamma_{b,i}) = 10^{-3}$, where $\gamma_{b,i} \leq \gamma < \gamma_{b,i+1}$

The average BER is also taken over the Rician fading as

$$\bar{P}_b = \sum_{i=1}^{N_{\text{mode}}} P_b(\gamma | \text{mode } i) \Pr(\text{mode } i \text{ is selected}) \quad (11)$$

where $P_b(\gamma | \text{mode } i)$ is computed using (4) for $g_i \leq g_J < g_{i+1}$, $i = 1, L, N_{\text{mode}}$.

The jammer's goal is to minimize the data rate of the transmitter. The optimum jamming probability b can be chosen from 0 to 1. When the transmitted signal is jammed with E_b/N_J and the jamming probability b is less than 1, the instantaneous bandwidth efficiency of each ACM mode is computed as

$$R(g_i) = b \times R(g_i | J) + (1 - b) \times R(g_i | UJ) \quad (12)$$

where b is the probability of the channel being jammed, ranging from 0 to 1, and $R(g_i | J)$ and $R(g_i | UJ)$ are the bandwidth efficiency when the channel is being jammed and not jammed,

respectively.

If the JSI is known at the receiver, i.e., E_b/N_J can be determined, then the spectrum efficiency under jamming is computed by using theorem 1, $E_s/(N_J/b)^3 g_i$, to check if the selected ACM mode can be employed. Theorem 1 can be simplified as $b^3 g_i/(E_s/N_J)$, where g_i is the computed cutoff SNR under AWGN of ACM mode i . If the condition holds, then the cutoff SJNR can be computed using (7). Thus the selected ACM mode can be employed under jamming with given E_b/N_J . If the ratio of g_i and E_b/N_J does not satisfy the inequality, then the selected ACM mode cannot be employed.

5. Result and Discussions

This section discusses the numerical results of the ACM bandwidth efficiency and ACM BER under the Rician fading of factor $K = 5$. Both the no-jamming case and the jamming case with $E_b/N_J = 10$ dB and jamming probability $b = 1$ are considered.

Fig. 4 shows the instantaneous spectral efficiency versus SNR $g = E_b/N_0$ in dB for the no-jamming case (Case A), jamming with JSI case (Case B), and jamming without JSI case (Case C). No fading is assumed. Observe that there are six noticeable steps and one unnoticeable step at g equal to 7 dB for Case A. This is because ACM modes 8 and 9 produce the same bandwidth efficiency, which is consistent with the results in Table 2. Therefore, it would be better not to employ mode 9 if the goal is to achieve a higher bandwidth efficiency. However, from Fig. 2, mode 9 can achieve a lower BER than mode 8 at a higher SNR. For example, if the target BER is 10^{-4} , it would be better to employ mode 9. Two ACM modes 5 and 6 are not employed as stated earlier because they show worse bandwidth efficiency and require a higher SNR than mode 4. Also, observe that the maximum instantaneous bandwidth efficiency is 3 bits/s/Hz, which can be achieved with 8PSK of no coding when the instantaneous SNR is greater than 10 dB.

Observe also in Fig. 4 that Cases B and C under jamming show a similar performance, but the maximum reachable instantaneous bandwidth efficiency is only 2 bits/s/Hz. This is because mode 10 shows a BER floor higher than 10^{-3} in Fig. 2, even for a very strong $E_b/N_0 = 10$ dB, and therefore, mode 10 cannot be used. The bandwidth efficiency of 2 bits/s/Hz can be achieved by employing QPSK with no coding.

Observe also in Fig. 4 that Case C (without JSI) shows a performance close to Case B (with JSI), even if JSI is not available. This is surprising and encouraging. Note also that the proposed

algorithm does not need channel estimation, which simplifies the receiver processing significantly. The time delay caused by searching for a proper ACM mode with BER criteria may be acceptable in many applications, e.g., a disruption/delay tolerant network (DTN) [12]–[14]. It will take less than an eight-frame interval delay to update the ACM mode if there are eight possible ACM modes in total, because each frame size can be sufficient to generate a BER test, e.g., 100,000 bits per frame, and eight frames take only 80 ms for 10 Mbps of data rate. Therefore, the proposed algorithm in Fig. 3 may be usable for future military satellite communications (MILSATCOM) waveform designs.

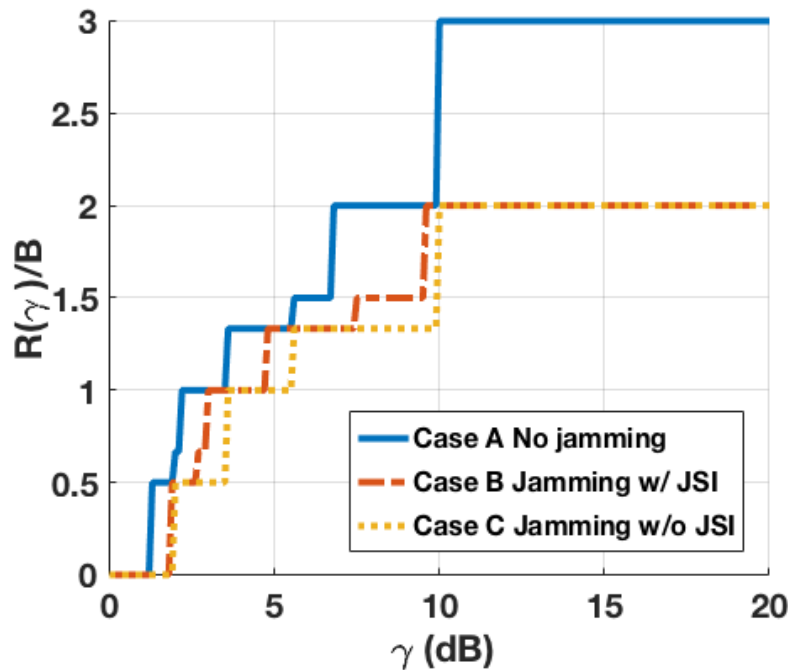


Fig. 4: Instantaneous spectral efficiency versus $g = E_b/N_0$ in dB for no jamming (Case A), jamming with JSI (Case B), and jamming without JSI (Case C). No fading is considered.

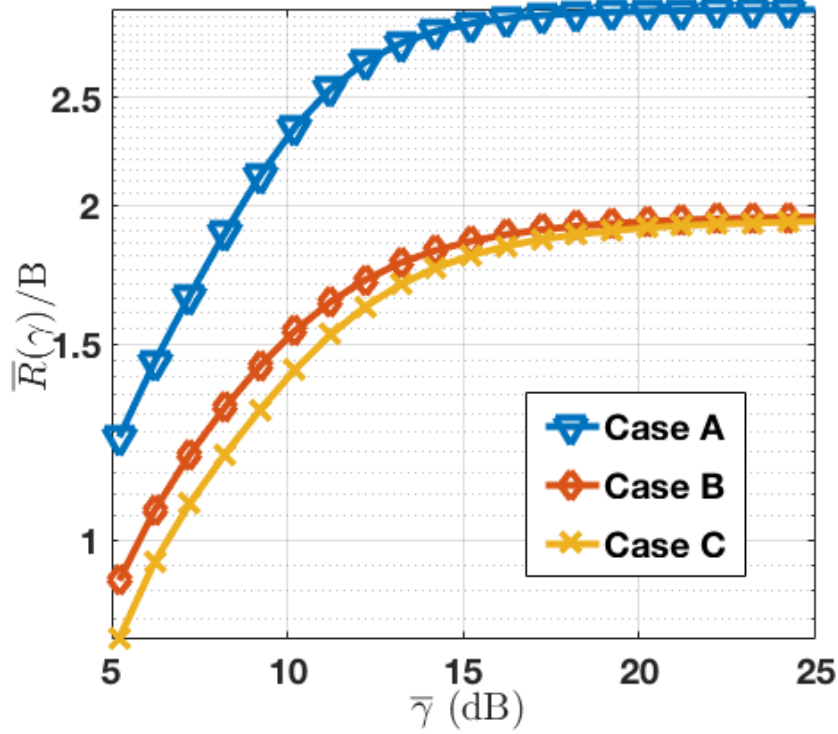


Fig. 5: Average bandwidth efficiency comparisons of Cases A, B, and C. Average is taken over Rician fading of Rician factor $K = 5$.

Fig. 5 shows the average bandwidth efficiency versus the average received SNR $\bar{\gamma}$ and presents the results of Cases A, B, and C. Observe again in Fig. 5 that Case C (without JSI) shows a performance close to Case B (with JSI), even if JSI is not available, and Case C shows almost the same performance as Case B when $\bar{\gamma} \geq 30$ dB for a given scenario of jamming in this report.

Fig. 6 shows the average BER versus $\bar{\gamma}$ and compares the results for Cases A, B, and C. Again, the average is taken over the Rician fading. Observe in Fig. 6 that Case A shows the smallest (best) average BER when $\bar{\gamma}$ is sufficiently higher than 32 dB because Cases B and C show the BER floor due to jamming for a high SNR region. Observe that when the average SNR is lower than 30 dB, Case C without JSI shows a smaller BER than Case B and even Case A. This is because in Case A, all eight of the ACM modes are considered, while in Case B, the 8PSK modulation with no coding is deleted since the BER target cannot be achieved under jamming. And in Case C (refer to Table 5), only four of the ACM modes are used: QPSK with code rates of 1/4, 1/2, and 2/3, and 8PSK with a code rate of 2/3 (refer to Theorem 1). In addition, the first region in Case C is considered as a no-transmission region because the lower SNR boundary cannot achieve the target BER. Thus, the average BER of Case B is higher than that of Case C, but Case B has higher

bandwidth efficiency than Case C. And since the instantaneous BER under fading is set to be less than or equal to a maximum allowable BER 10^{-3} , the average BER of Case B is acceptable. This report focuses more on the bandwidth efficiency criteria rather than BER.

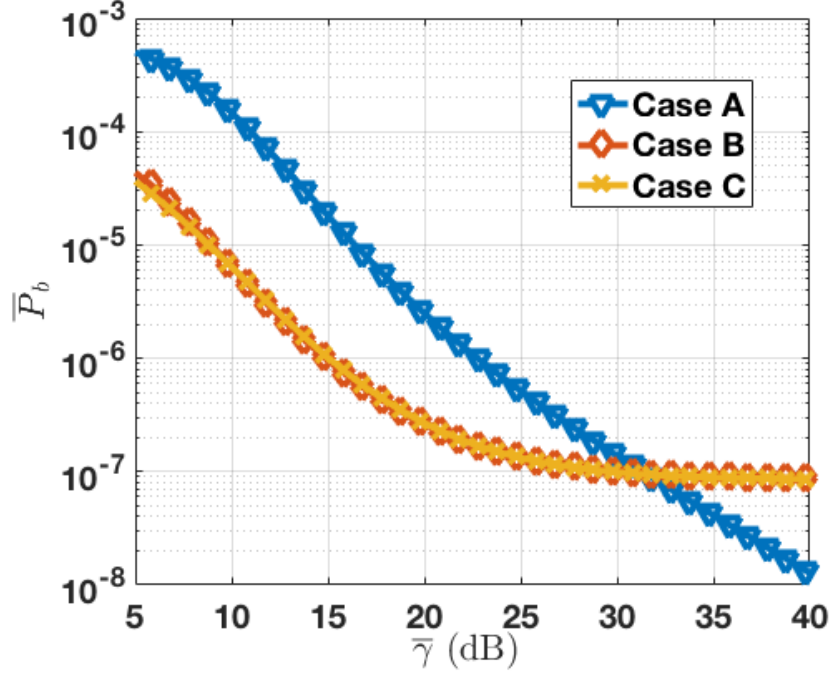


Fig. 6: Average BER comparisons of Cases A, B, and C. Average is taken over Rician fading of Rician factor $K = 5$.

Observe also in Fig. 6 that the average BER of Cases B and C are bounded (flat line) as the SNR is increasing, while that of Case A is consistently decreasing. This is because Cases B and C are under jamming, while Case A is under no jamming. The probability density function of the instantaneous SNR in a Rician fading channel of Case A, written as (1), is a function of $\bar{\gamma}$, while the probability density function of SJNR in a Rician fading channel for Cases B and C is a function of $\bar{\gamma}_J$.

Fig. 7 shows a comparison between $\bar{\gamma}$ and $\bar{\gamma}_J$ whose relationship is described in (3). Observe that as E_b/N_0 increases, $\bar{\gamma}$ is proportionally increasing since it is a function of E_b/N_0 , while $\bar{\gamma}_J$ is saturated because it is limited by $E_b/N_J = 10$ dB. Since $\bar{\gamma}_J$ is slowly increasing when compared to $\bar{\gamma}$, it affects the average BER of Cases B and C to flatten, as shown in Fig 6. In other words, under a jamming environment, the average BER is limited by $E_s/N_J = (\log_2 M)E_b/N_J$.

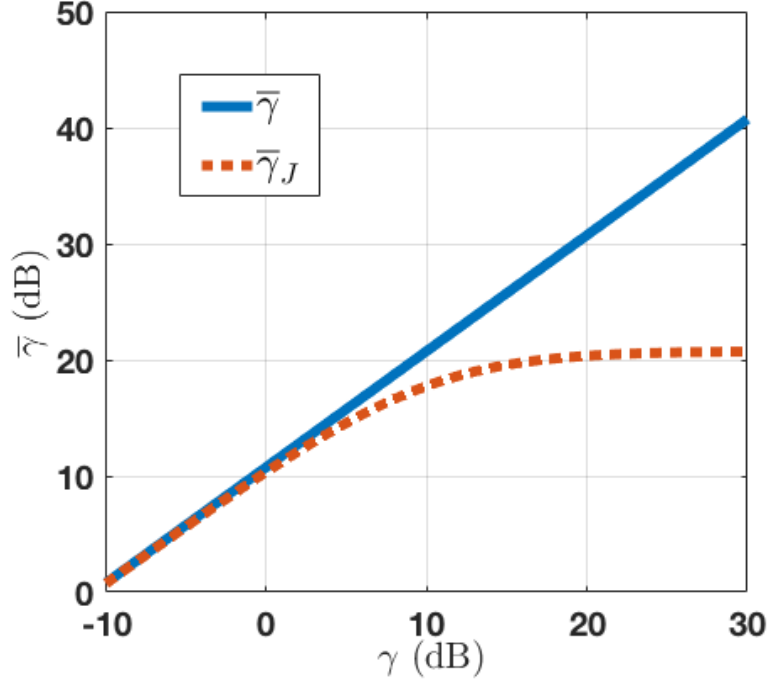


Fig. 7: Comparison of $\bar{\gamma}$ and $\bar{\gamma}_J$.

Fig. 8 presents BER versus $g_b = E_b/N_0$ for the second set of twenty ACM modes under AWGN. These ACMs are combinations of two modulations (QPSK and 8PSK) and the LDPC FEC of 12 code rates [9]. The crossing points at $P_b(g) = 10^{-5}$ marked by red triangles are the lower boundaries of $g_{b,i}$ for ACM mode i under the AWGN when there is no jamming. The LDPC code word length used in simulation is $n = 64,800$, as stated in DVB-S2 [9, p.13]. Table 3 lists the corresponding 20 modes of the adaptive code modulations. The SJNR from column 5 in Table 3 is computed from (7).

Observe that modes 10, 11, and 12 (QPSK with 8/9 and 9/10 code rate and QPSK no coding) have a higher cutoff SNR, while their bandwidth efficiencies are lower than mode 13 (8PSK with 3/5 code rate). Thus, for the no-jamming case (Case A), modes 10 to 12 are deleted.

For Case B, modes 18 to 20 have a cutoff SNR (no jamming) lower than $b E_b/N_J$. These cutoff values $g_{b,i,J}$ cannot satisfy the target BER = 10^{-5} from (7) or Theorem 1. Modes 10 to 12 have lower bandwidth efficiency but higher cutoff SNR values than mode 13. Therefore, six ACM modes in Case B are deleted. For Case C, it is assumed that the BER after LDPC decoding is still a type of $Q(a)$ function. For calculation purposes, the signal bit energy-to-jamming power spectral density $E_b/N_J = 10$ dB is used; however, the receiver does not have the jamming state information in this

case. The calculation uses the proposed algorithm in Fig. 3 to determine the ACM modes for each region by testing the cutoff SNR obtained from Case A in Table 3. Because finding the true BER using LDPC decoding simulation is too time consuming, (7) is used to determine the minimum SNR that can achieve the target BER. The receiver compares the input cutoff SNR (obtained from Case A) one by one, with the computed SJNR using (7).

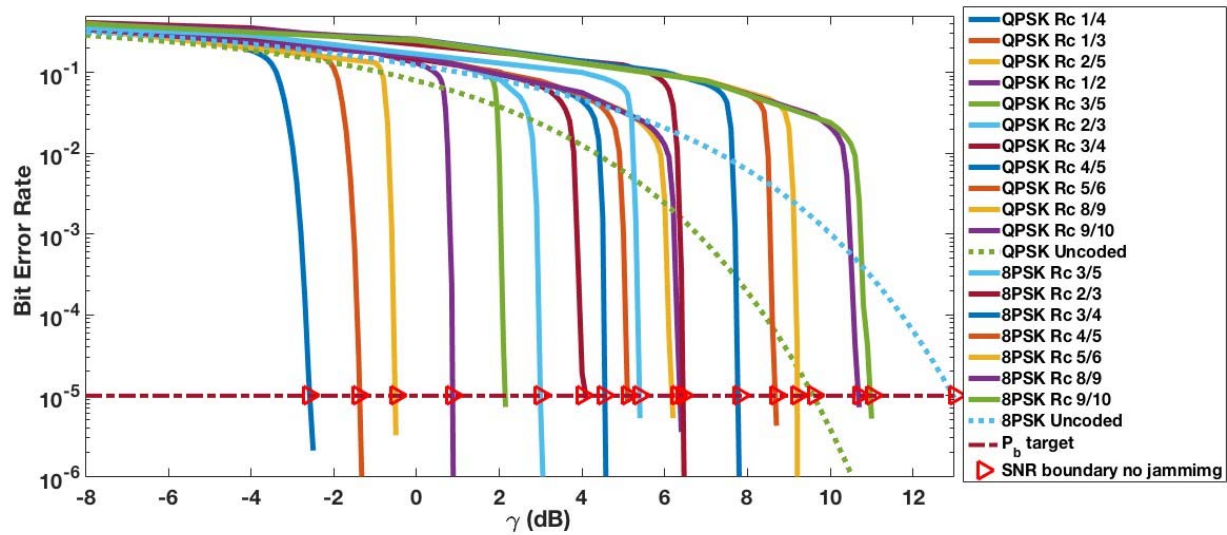


Fig. 8: Plots of bit error rate $P_b(g)$ versus $g = E_b/N_0$ in dB for 20 ACM modes applied FEC LDPC coding under AWGN, assuming no jamming. Crossing points at $P_b(g) = 10^{-5}$ are marked by triangles in red.

Fig. 9 shows the instantaneous spectral efficiency versus SNR $g = E_b/N_0$ in dB for the ACM with LDPC for Cases A, B, and C. Observe similar observations from Fig. 4.

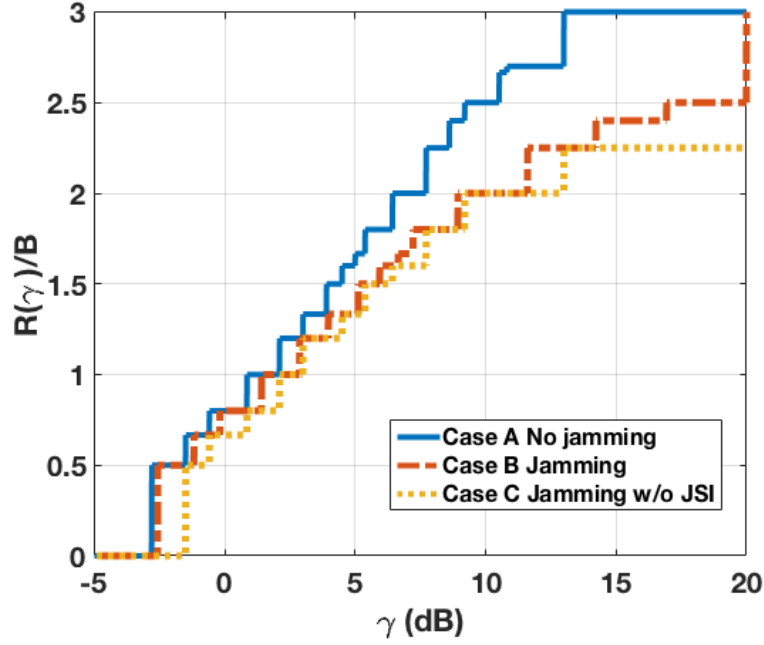


Fig. 9: Instantaneous spectral efficiency versus $g = E_b/N_0$ in dB applied FEC LDPC from Table 3, for no jamming (Case A), jamming with JSI (Case B), and jamming without JSI (Case C). No fading is considered.

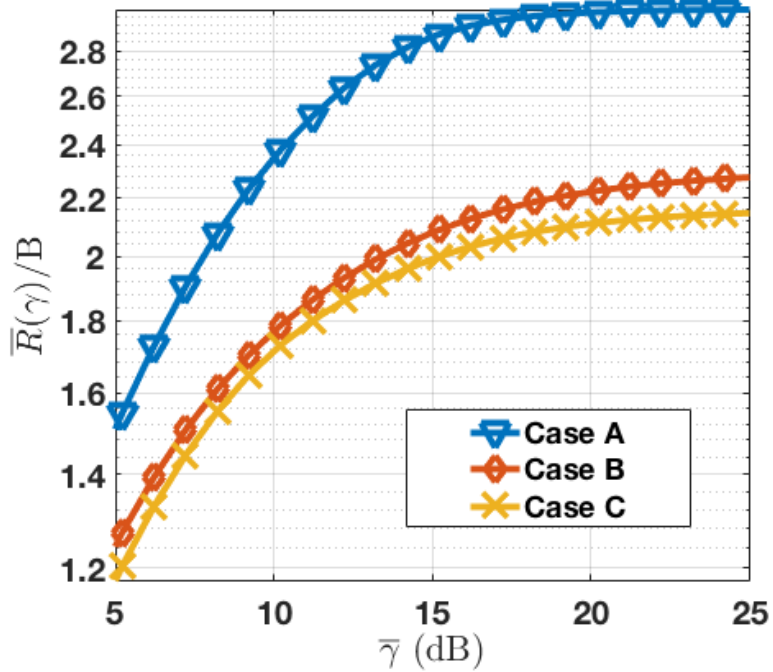


Fig. 10: Average bandwidth efficiency comparisons of Cases A, B, and C applied FEC LDPC from Table 3. Average is taken over Rician fading of Rician factor $K = 5$.

Fig. 10 shows the average bandwidth efficiency versus the average received SNR \bar{g} for the

ACM with LDPC under a Rician fading of Rician factor $K = 5$. Similar observations can be seen in Fig. 5. However, there is a small gap between Case C and Case B when \bar{g} is high. Also, observe that the overall average bandwidth efficiency of the LDPC ACM is higher than that of the convolutional FEC ACM, even if a stricter BER equal to 10^{-5} is applied to the LDPC ACM. This is because the LDPC FEC ACM can have higher code rate than the convolutional FEC ACM considered in this report.

A jammer can adjust the jamming probability b based on the jamming power. If the jammer has sufficient power to jam the channel, e.g. E_b/N_J is 5 dB (strong jamming), then the jammer tends to use broadband jamming, e.g., jamming all channels. However, if the jamming power is weak or the SNR is strong, then jammer will use a single-band tone. By arranging the jamming probability and Rician factor, the optimum jamming probability can be determined.

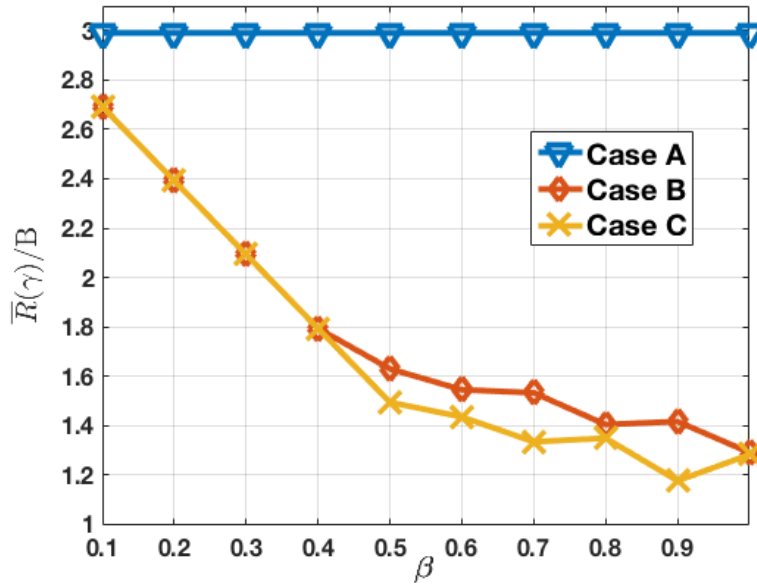


Fig. 11: Average bandwidth efficiency comparisons of Cases A, B, and C versus PBTJ fraction b . Average is taken over Rician fading of Rician factor $K = 0.1$ with $E_b/N_J = 5$ dB, E_b/N_0 target = 10 dB, and BER target = 10^{-3} .

Fig. 11 shows the average spectrum efficiency when the probability of jamming ranges from 0.1 to 1 with $E_b/N_J = 5$ dB, Rician factor $K = 0.1$, and target E_b/N_0 target = 10 dB. The Rician factor is set to 0.1 to demonstrate the channel close to Rayleigh fading when LOS is not present. Observe that Case A has constant bandwidth efficiency because the BER and E_b/N_0 are fixed.

For Cases B and C, the bandwidth efficiency is decreasing as the jamming probability increases, and the lowest bandwidth efficiency occurs when b approaches 1. This is because higher ACM modes cannot be employed under a strong jamming condition. Thus, when the jammer increases the jamming frequency, most of the data are likely to be in error for a binary modulation. This shows that if the jammer has sufficient jamming power, then it is more efficient for the jammer to use a broadband jamming technique in order to minimize the data rate transfer.

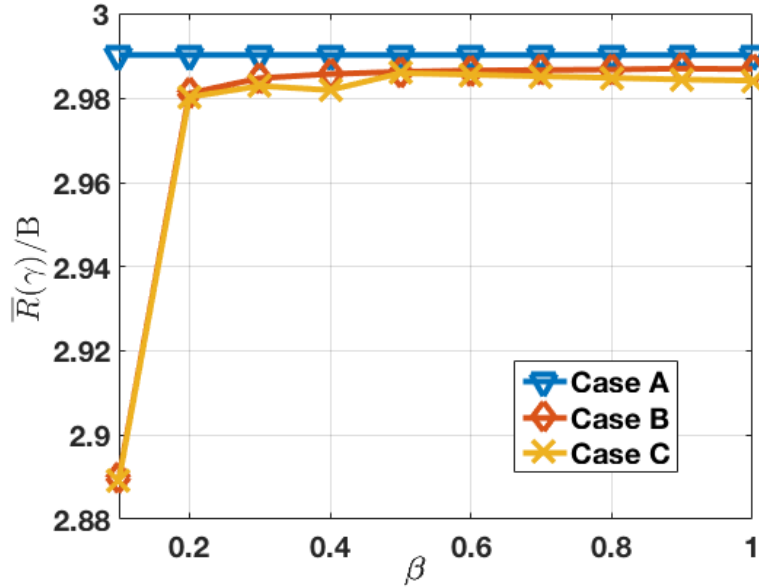


Fig. 12: Average bandwidth efficiency comparisons of Cases A, B, and C versus PBTJ fraction β . Average is taken over Rician fading of Rician factor $K = 5$ with $E_b/N_J = 20$ dB, E_b/N_0 target = 10 dB, and BER target = 10^{-3} .

Fig. 12 shows the average spectrum efficiency when the probability of jam is ranging from 0.1 to 1 with $E_b/N_J = 20$ dB, Rician factor $K = 5$, and target E_b/N_0 target = 10 dB. This is the case when the jamming signal is weak. Observe that the spectrum efficiency of Cases B and C, when the jamming is present, are close to that of Case A, which is an unjammed case. The lowest bandwidth efficiency occurs when beta approaches 0. This can be explained by using Theorem 1 and equation (12). From (12), the spectrum efficiency of jamming $R(g_{i,J}/J)$, and unjamming, $R(g_i/UJ)$, cases are based on Bernoulli probability. As the jamming probability increases, the

ratio of unjammed spectrum efficiency decreases. Since the BER and E_b/N_0 are fixed, the unjammed spectrum efficiency is constant. Thus, only the jammed spectrum efficiency varies. From Theorem 1, high ACM modes are likely to be employed as β increases. In this case, when the jamming signal is weak, a higher ACM mode can be employed when b is approaching 1; therefore, the average spectrum efficiency is increasing. It can be concluded that when the jammer has less jamming power, the most effective jamming probability is 0.1. This shows that a jammer tends to use single-band jamming when there is insufficient power.

Appendix A describes the front-panel block diagrams of USRP 2932 used for verification of concepts in the research project through hardware radio communications systems testing. Three USRPs 2932 are used: one for a desirable signal transmitter, another for a receiver, and the third for a jamming signal transmitter. Test results did not match with theoretical results, even for a very simple setup, e.g., a QPSK modulation under an additive white Gaussian noise channel. Appendix A presents the rationales why analytical and test results do not agree with each other, and demonstrates also the necessary calibration steps for the experimental and theoretical results to meet together.

Appendix B describes the block diagrams in the back-panel of USRP hardware radio communications system. The observations and experiences obtained through testing with the hardware wireless communications systems are expected to be useful for future testing with USRPs.

6. Conclusions

This report studied an adaptive code modulation to enhance the bandwidth in a bandwidth-constrained and power-constrained communication system environment. The results here can be useful for designing future satellite communication systems under jamming environments. The proposed BER-based ACM algorithm, even with no jamming state information, can show a bandwidth efficiency performance close to that of the ACM mode with JSI. And the average BER of the proposed BER-based ACM algorithm shows the best BER performance out of the three ACM schemes (ACM under AWGN, ACM under jamming with no JSI, and ACM under jamming with JSI) when the average SNR is small, such as 30 dB.

For future work, it is desirable to design an ACM where the average BER is within a small upper and lower BER bound from the target BER.

Finally, for verification of concepts in the research project through hardware radio communications systems testing, three USRPs 2932 were used: one for a desirable signal transmitter, another for a receiver, and the third for a jamming signal transmitter. Test results with USRPs did not match with theoretical results at the beginning of test. This report found the rationales. First, the AWGN at transmitters should not be included. Second, the noise power spectral density at a receiver should be calibrated because the front panel of USRP 2932 receiver provides incorrect bit energy to noise density ratio information. This report demonstrated the necessary calibration steps for the experimental and theoretical results to meet together.

The observations and experiences obtained through testing with the hardware wireless communications systems are expected to be useful for future testing with USRPs.

References

- [1]. Ellils, J. D. and Pursley, M. B., “Integration of adaptive modulation and channel coding with fountain coding for packet radio systems,” *IEEE Transactions on Communications*, vol. 63, no. 5, pp. 1510–1521, Feb. 2015.
- [2]. Pursley, M. B. and Royster, T. C., “Adaptive-rate nonbinary LDPC coding for frequency-hop communications,” IEEE Military Communications Conference, San Diego, CA, pp. 1-6, November 16-19, 2008.
- [3]. Goldsmith, A., *Wireless Communications*, pp. 78-79, Cambridge University Press, 2005.
- [4]. Wolf, B. J. and Huang, J. C., “Implementation and testing of the Protected Tactical Waveform (PTW),” IEEE Military Communications Conference, Tampa, FL, pp. 181-186, October 25-28, 2015.
- [5]. Royster, T. C. and Streitman, J., “Performance considerations for protected wideband satcom,” IEEE Military Communications Conference, Tampa, FL, pp. 175-180, October 25-28, 2015.
- [6]. Glaser, M., Greiner, K., Hilburn, B., Justus, J., Walsh, C., Dallas, W., Vanderpoorten, J., Chuang, J.-C., and Sunshine, C., “Protected MILSATCOM Design for Affordability Risk Reduction (DFARR),” IEEE Military Communications Conference, San Diego, CA, pp. 998-1001, November 18-20, 2013.
- [7]. Cook, K. L., “Current wideband milsatcom infrastructure and the future of bandwidth availability,” IEEE Aerospace and Electronics Systems Magazine, vol. 25, no. 12, pp. 23–28, 2010.
- [8]. European Telecommunications Standards Institute (ETSI), “Digital video broadcasting (DVB): second generation framing structure, channel coding and modulation systems for

broadcasting, interactive services, news gathering and other broadband satellite applications (DVB-S2), Final Draft ETSI EN 302 307 v1.2.1,” p. 13, 2009-04.

[Online]. Available: <http://www.etsi.org>,

http://www.etsi.org/deliver/etsi_en/302300_302399/302307/01.02.01_40/en_302307v010201o.pdf.

- [9]. European Telecommunications Standards Institute (ETSI), “Digital video broadcasting (DVB): interaction channel satellite distribution systems European standard (telecommunications series), ETSI EN 301 790 v1.4.1,” p. 13, 2005-09.

[Online]. Available: <http://www.etsi.org>,

http://www.etsi.org/deliver/etsi_en/301700_301799/301790/01.04.01_60/en_301790v010401p.pdf.

- [10]. Cioffi, John, “System Design with Codes,” Digital Communication: Signal Processing Course, 2016. [Online]. Available: <http://web.stanford.edu/group/cioffi/book/chap10.pdf>.

- [11]. Moon, T. K., Error correction coding: Mathematical Methods and Algorithms, p. 499, Wiley-Interscience, 2005.

- [12]. Burleigh, S., “Contact graph routing,” NASA/JPL, California Institute of Technology, posted July 8, 2010. [Online]. Available: <https://tools.ietf.org/html/draft-burleigh-dtnrg-cgr-01>.

- [13]. Burleigh, S., “The ring road: Cubesats + dtna proposed architecture for cheap, reliable network services for remote regions,” Space Technology Innovations Conference, posted January 24, 2014. [Online]. Available: <https://www.youtube.com/watch?v=4RusR2PiqPs>.

[14]. The Consultative Committee for Space Data Systems (CCSDS), “The SDS Bundle Protocol Specification, “Recommended Standard, CCSDS 734.2-B-1, Blue Book,” ” pp. E-1 – E-2, September 2015.

[Online]. Available: <http://www.ccsds.org>,

<https://www.google.com/#q=Recommended+Standard,+CCSDS+734.2-B-1,+Blue+Book>.

Appendix A: USRP Front Panel Block Diagrams

APPENDIX A - LIST OF FIGURES

| | |
|---|----|
| Fig. A-1. Block diagram of front panel of transmitter (TX)..... | 31 |
| Fig. A-2. Block diagram of front panel of receiver (RX)..... | 34 |
| Fig. A-3. BER results with calibrated noise power and calibrated SNR equal to SNR2 under no jamming..... | 38 |
| Fig. A-4. Experimental BER results with calibrated SNR and transmitter gain as a parameter... | 40 |
| Fig. A-5. Experimental results with jamming..... | 41 |
| Fig. A-6. Short-distance experiment setup..... | 42 |
| Fig. A-7. Long-distance experiment setup..... | 42 |
| Fig. A-8 Experiment devices used..... | 43 |

Preface

Appendix A of this report presents the observations and experiences obtained during the test from October 2016 to May 2017 on a Universal Software Radio Peripheral (USRP) front panel block diagram related to the research project “Optimum Boundaries of Signal-to-Noise Ratio for Adaptive Code Modulations,” U.S. Air Force Research Laboratory, Grant Award Number FA9453-16-1-0049, using three 2932 USRPs—one for a transmitter (TX), another for a receiver (RX), and the third for a jammer transmitter. Test results, even for a very simple setup, e.g., QPSK modulation under an additive white Gaussian noise (AWGN) channel, did not match with theoretical results. This report finds and presents the rationale for why the analysis and test results do not agree with each other, and also demonstrates the necessary calibration steps in order for agreement to occur. It is expected that observations and experiences outlined in this report will be useful for other ongoing and future tests involving USRPs.

Sections of the block diagrams in Appendix A are referred to by their **red** numbers and are explained below.

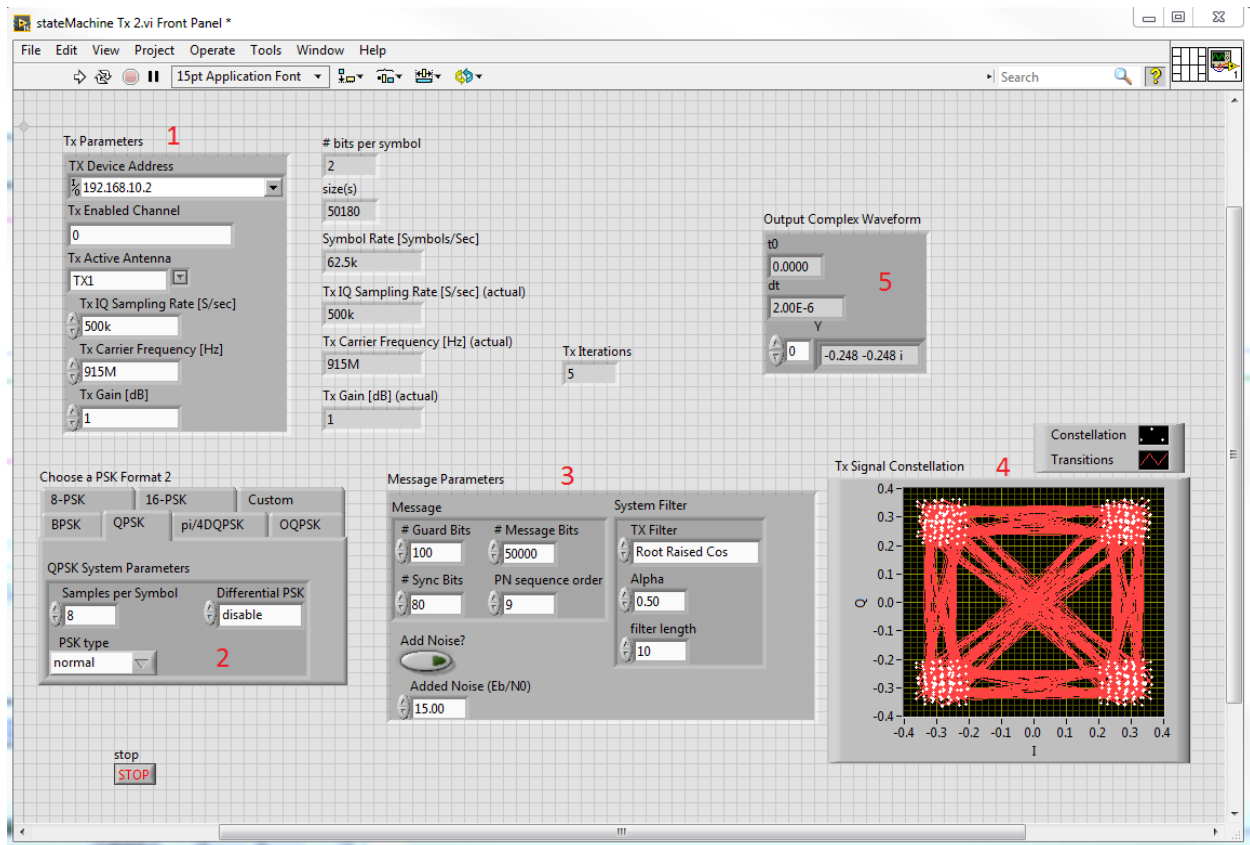


Fig. A-1. Block diagram of front panel of transmitter (TX).

Front Panel of Transmitter Shown in Fig. A-1

Section 1: Transmitter Parameters

TX Device Address: This is an Internet Protocol (IP) address of a Universal Software Radio Peripheral (USRP) transmitter. This transmitter address is different from that of a receiver because the TX and RX share a personal computer (PC), and each one should use its own address for proper communications. If both TX and RX USRPs use the same IP address, then the common PC will be confused about where the signal is coming from and where the signal is sent to.

Tx Enabled Channel: Channel “0” is the default and the only option in USRP 2932.

Tx Active Antenna: TX1 is the only option in USRP 2932.

Tx IQ Sampling Rate [S/sec]: This value indicates the sampling rate.

Tx Carrier Frequency [Hz]: This value indicates the carrier frequency.

Tx Gain: This value indicates the gain set for the transmitter. Higher gain means higher transmitting power.

Bits per Symbol: For example, a quadrature phase shift keying (QPSK) and a 16-ary phase shift keying (16PSK) modulations carry 2 bits and 4 bits per symbol, respectively.

Size(s): Number of bits transmitted for test, including guard bits and sync bits.

Symbol Rate [Symbols/Sec]: This value indicates the symbol rate.

Tx Sampling Rate [S/sec] (actual): This value indicates the actual sampling rate.

Tx Carrier Frequency [Hz] (actual): This value indicates the actual carrier frequency.

Tx Gain [db] (actual): This value indicates the actual gain set for the transmitter.

Tx Iterations: Number of iterations that the same information block is sent repeatedly by using a feedback loop.

Note: If a block in the transmitter front panel, shown in Fig. A-1, indicates a number in gray color, then this means that the output is in default, as defined by the USRP 2932 device. For example, even if Tx Gain [dB] is set to 1000 dB, the Tx Gain [dB] (actual) is only 30 dB because the maximum transmitter gain of a USRP 2932 is 30 dB. For another example, even if the Tx Carrier Frequency [Hz] is set to 1000 G, the Tx Carrier Frequency [Hz] (actual) is 4.4 GHz because the USRP 2932 device supports only 400 MHz to 4.4 GHz.

Section 2: Choose a PSK Format

This block indicates the desired PSK format. Only QPSK or 16PSK were used because, for some reason, 8PSK was not working properly in the acquired USRPs.

Section 3: Message Parameters

Guard Bits: This value indicates the number of guard bits between block.

Sync Bits: To secure synchronization between a TX USRP and a RX USRP, a certain number of bits are required. This report uses 80.

Message Bits: The PN sequence period is $2^{\text{PN sequence order}} - 1$. If the PN sequence period is longer than the # Message Bits, then the USRP transmitter takes the first # Message Bits from the generated PN sequence. If not, the PN sequence is repeated and then # Message Bits are taken from the repeated PN sequence.

PN Sequence Order: The generated or transmitted bit sequence is a pseudo-random one, and the randomness is controlled by this parameter. This report uses PN sequence order equal to 9. The PN sequence will be repeated every $2^9 - 1$.

Add Noise?/Added Noise (Eb/N0): If this button is on, then an extra additive white Gaussian noise is added at the transmitter (not at the receiver) before sending the signal with the chosen

Added Noise (E_b/N_0) parameter. This causes the bit error rate (BER) test results to be higher than the theoretical BER results. This fact was determined later on, after spending several months, since the lab test started in October 2016. Thermal noise is added just before demodulation at a receiver for analysis. Therefore, in this report, this button was turned “off,” after observing a significant difference between the measured and theoretical BERs. In other words, no extra transmit noise is necessary at a USRP transmitter.

Tx Filter: The three options on this filter are No Filter, Root Raised Cosine, and Raised Cosine. This report uses the Root Raised Cosine filter at both the transmitter and the receiver.

Alpha: This is the “roll-off” parameter between 0 and 1, where 1 shows the best eye diagram performance, i.e., a wider and clearer open-eye diagram; however it requires a wider bandwidth. This report uses an Alpha equal to 0.5.

Filter Length: This is the length of the filter.

Section 4: Transmitter Signal Constellation

This plot shows the constellations and transition trellises for the selected modulation as the transmitter sends the data bits. QPSK modulation was selected, and the QPSK constellations are shown here.

Section 5: Output Complex Waveform

This section provides a description of the signal for the USRP device.

t0: This is the time stamp representing the time at which the signal measurement starts.

dt: This describes the difference in milliseconds between two adjacent samples in the signal, i.e., sampling interval.

Y: This represents the sample values.

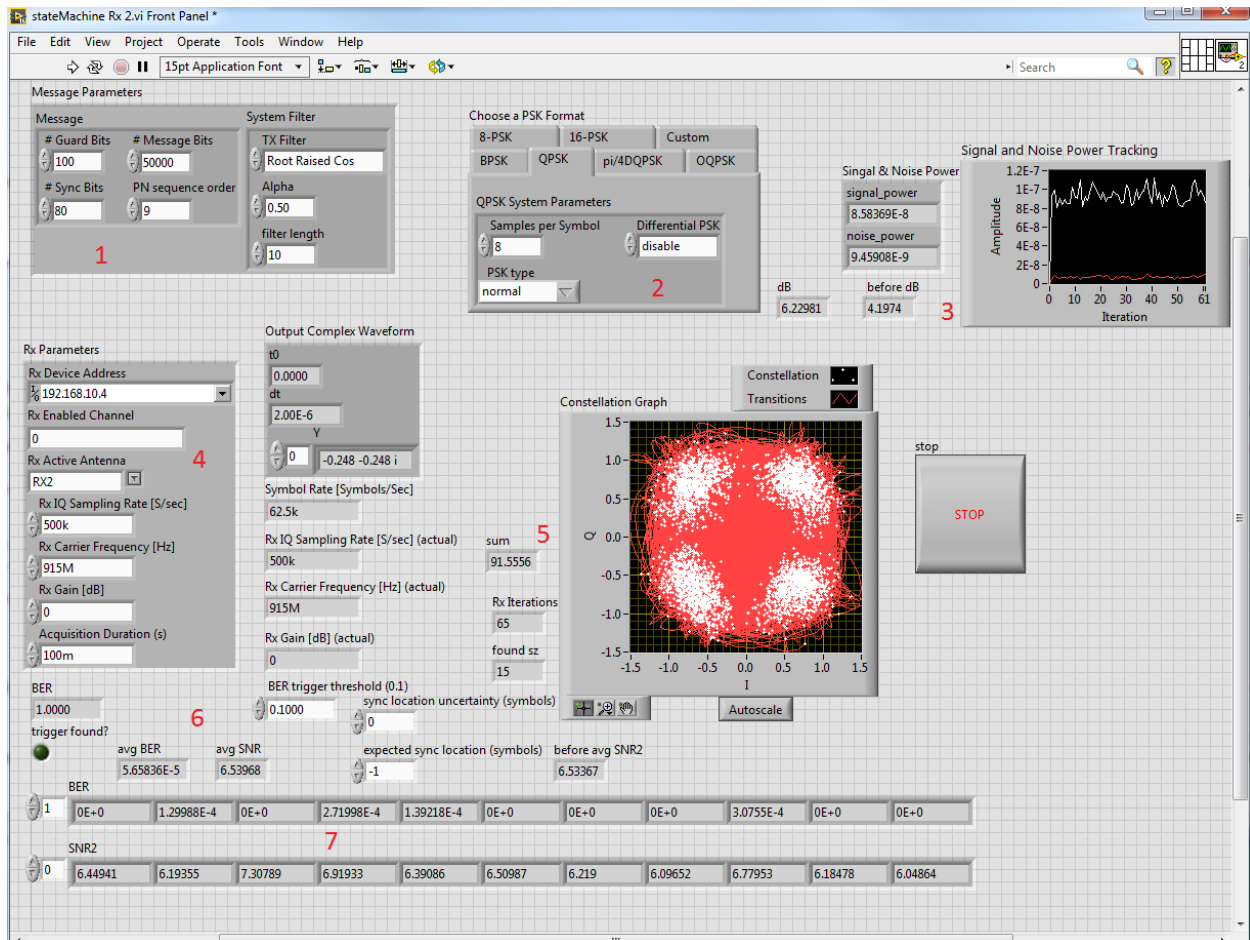


Fig. A-2. Block diagram of front panel of receiver (RX).

Front Panel of Receiver Shown in Figure A-2

Section numbers shown in red in the block diagram of the receiver front panel in Fig. A-2 are explained below.

Section 1: Message Parameters

Message parameters in this section for the receiver should match with those in Section 1 for the transmitter.

Section 2: Choose a PSK Format

The PSK format in this section for the receiver should match with those in Section 2 for the transmitter.

Section 3: Signal and Noise Power Tracking

Signal & Noise Power: The signal and noise power data in this box on the left are plotted in the box on the right.

Signal and Noise Power Tracking: This is a plot of the signal and noise power data values found in the box on the left.

dB: This represents the signal-to-noise ratio (SNR) converted to dB, i.e., $10 \log_{10} SNR$.

Before dB: This is the SNR before dB, which is measured with the inbuilt function N_0 , which represents a thermal noise power spectral density at the RX.

Note on Received Signal Power: The values of signal power in the box named “signal_power” are **reliable** because the values meet all the expected results for the following experiments:

- The received signal power is proportionally changing to the TX gain. In other words, the received signal power increases when the TX gain increases, and vice versa.
- The received signal power decreases as the distance between the TX and the RX USRP increases for a given TX power.
- The received signal power gets stronger when another USRP radio signal (e.g., a jamming signal) is turned on.
- The received signal amplitude versus iteration is plotted in the right-side block during signal transmission. When a hand is waved between a USRP TX antenna and a USRP RX antenna, fluctuation was observed in the chart, and when a hand is moved away, the fluctuation in the received signal stops immediately.

Note on Noise Power: The noise power in Section 3 is **not** reliable. Results also showed that the values of SNR “dB” and “before dB” are not reliable. The values (noise power, before dB, and dB) shown in Section 3 are for demonstration purposes only and do not represent true values. The following observations were made for justifying this claim.

1. Observation of Noise Power

The AWGN noise power from the USRP device is intended to be **constant** or **approximately constant** because the room temperature in the lab is not changing rapidly. However, it was observed that the noise power increases when the TX gain increases. In addition, it was observed that the SNR ratio becomes a constant number, regardless of the TX gain because the noise power increases proportionally to the received signal power. Therefore, it was observed that the values of “dB” and “before dB” are almost the same, even if different transmitting gain is applied.

2. Reason for Incorrect Noise Power

The statements in this and the following paragraph are from email discussions with a National Instrument technician. The USRP 2932 is not a calibrated device, and there are possible external noise sources that contribute to the unstable E_b/N_0 ratio calculation. For example, noises in the local oscillator (LO) output are fed into the TX and RX USRPs, and this can cause a very narrowband noise near the center frequency during USRP signal acquisition and generation. This can cause a high BER because a constant noise power spectral density (PSD) is assumed for the SNR E_b/N_0 calculation in an USRP device, regardless of the actual noise PSD value. Hence, when external noises are injected from LOs to the USRP TX and RX signals, the value of E_b/N_0 in the display will be different from the actual value and can cause the BER curve versus E_b/N_0 to shift away from the theoretical one. In addition, instability in the reference clock can also cause a non-constant PSD level.

The USRP was originally intended to be used for prototyping wireless communications standards and formats. It was not intended for highly precise noise measurements and characterization, because the performance and specifications are not warranted. Measurement class instruments such as the PXIe-5644R or the PXIe-5668 are capable of performing these measurements because they have warranted specifications, but they are much more expensive.

3. How to Calibrate Incorrect Noise Power

This section presents a reasonable calibration method for the incorrect noise power problem described in the second reason above. This method is composed of two parts: first, a reasonable noise power is estimated by using a known theoretical BER vs SNR curve for a chosen M-ary phase shift keying (MPSK) from Section 2 shown in the TX and RX front panels; and second, the received signal power is detected and used. Calibration steps are detailed in below.

- Step 1.** Consider a QPSK modulation. Select the transmitting gain, then transmit a signal from a TX USRP to an RX USRP receiver. A TX USRP will transmit a 100 blocks of information per iteration, and a RX USRP will receive 100 blocks of information per iteration. Refer to “Rx Iterations” in Section 5 in Fig. A-2, which indicates the current iteration number.
- Step 2.** Read “signal_power” in the left box of Section 3 in Fig. A-2 and let x_1 denote the “signal_power.” Read “avg BER” in Section 6, and let ber_1 denote the “avg BER.”
- Step 3.** Apply ber_1 value obtained from Step 2 to a theoretical BER vs SNR curve for a QPSK modulation under an AWGN channel, and read the theoretical SNR value. Let snr_1 denote the theoretical SNR.
- Step 4.** Use the snr_1 obtained from Step 3 and the signal power x_1 obtained from Step 2, and compute the calibrated noise power as $n_1 = x_1/snr_1$.

Step 5. Repeat Steps 2 to 4 at least ten times, and compute the average noise power. Let *avg_noise_power* denote the average noise power. For example,

$$avg_noise_power = \frac{1}{10} \sum_{i=1}^{10} n_i.$$

Note that the values of *n_i* are stable, i.e., the variance of *n_i* is small. This is a positive sign of reliability in experiments. This *avg_noise_power* is used for all experiment plots.

Section 4: Rx Parameters

Rx Device Address: This Rx address in Fig. A-2 is different from the Tx address in Fig. A-1.

Rx Active Antenna: Two options, Rx 1 and Rx 2, are available in USRP 2932. Other receiver parameters are the same as those for the transmitter.

Acquisition Duration: If the acquisition time is longer, then the bigger portion of information block will be obtained.

Section 5: Constellation Graph

Constellation Graph: This shows a graph of the received signal constellation including noise.

Sum: This shows the sum of all incident SNRs.

Rx Iterations: This indicates the number of iterations performed at the receiver.

Found sz: This implies the array size for the average BER calculation.

Stop: This button stops the whole loop when a package is receiving.

Section 6: BER Trigger

BER: This is an instant BER.

Trigger Found?: If this indicator is on, then the package has been received correctly.

Avg BER: This represents the accumulated average BER.

Avg SNR: This is the average SNR.

BER Trigger Threshold: This number is set to a low number such as 0.1 because if it is set to a high number, e.g., 1, then the accuracy of the BER calculation decreases.

Sync Location Uncertainty (Symbols): The default number here is 0.

Expected Sync Location (Symbols): The default command to search the whole package is “-1.” If this number is a finite positive number, e.g., 10, then the sync location is located at the tenth symbol.

Before Avg SNR2: There is a nonzero chance that the first estimation of SNR is equal to a positive infinite number (+inf). If this happens, then this causes the “avg SNR” to equal +inf. Hence, the first estimation should be reset in this case. The value of “avg SNR” is the average value not including the first estimation.

Section 7: BER and SNR2

BER: All instantaneous BER values are saved into the BER array of size “found sz.” The “avg BER” is computed as the sum of the BER array contents divided by “found sz.”

SNR2: All instantaneous calibrated SNR values are saved into the calibrated SNR array of size “found sz.” The “avg SNR” is computed as the sum of the calibrated SNR array contents divided by “found sz.”

Experimental Results of Appendix A

BER results shown in Figs. A-3, A-4, and A-5 are compared with theoretical results for QPSK and 16PSK under AWGN, no jamming, and jamming where the noise power is calibrated and hence SNR is also calibrated. The parameters are listed below:

Parameters:

Sampling Rate: 500 K
 Carrier Frequency: 915 MHz
 Receiver Acquisition Duration: 100 ms
 TX and RX Distance: 83 cm, for “long distance” experiments shown in Figs. A-3 and A-4
 TX and RX Distance: 6 cm, for “short distance” experiments shown in Figs. A-3 and A-4
 Location Geometry: USRP TX, USRP RX, and USRP jammer located in a triangle position

Fig. A-3 shows BER results for QPSK and 16PSK modulations under no jamming with the calibrated SNR, referred to as SNR2, which is equal to the signal_power estimated from a built-in function in Section 3 of the Front Panel Receiver divided by the calibrated noise power described in Observation 3 on page 8. Solid lines represent theoretical BERs. Circles and stars represent the experimental BER results with the calibrated SNR. Circles represent the experimental BER results with the calibrated SNR when the distance between an USRP TX and an USRP RX is relatively short (6 cm) by varying the transmitter power gain as a parameter. Stars represent the experimental BER results with the calibrated SNR when the distance is relatively long (83 cm).

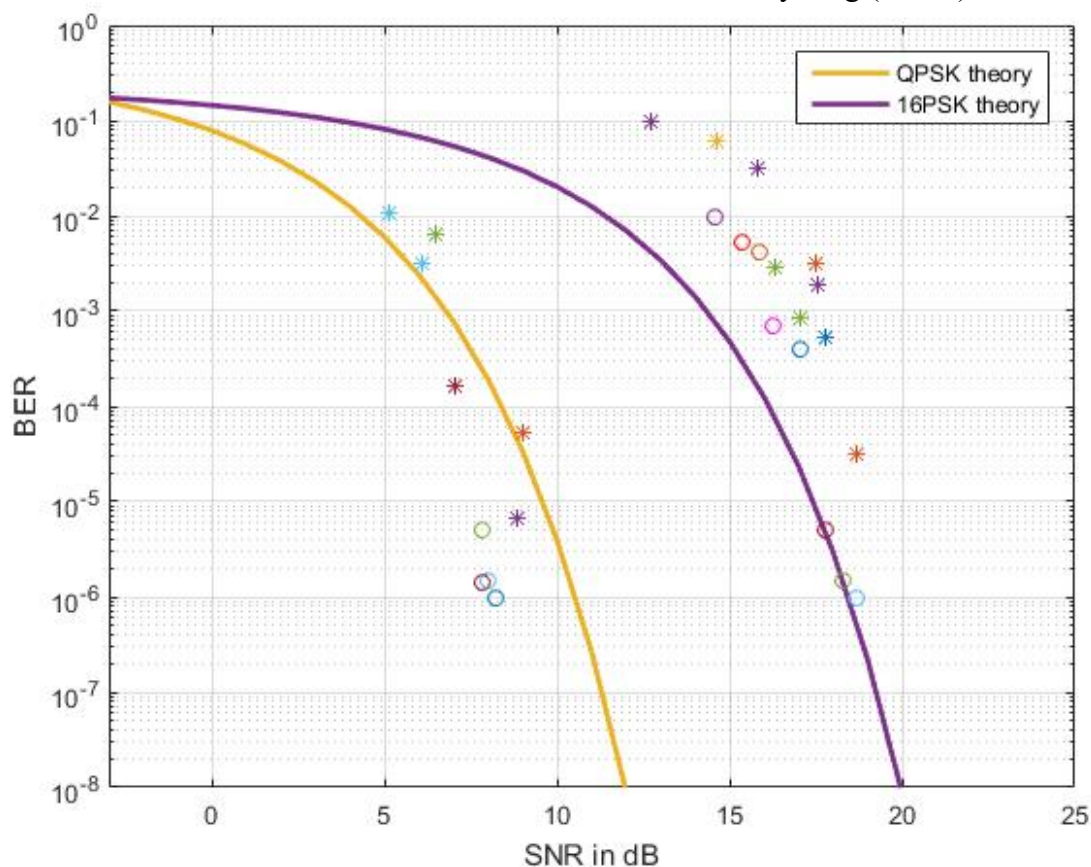


Fig. A-3. BER results with calibrated noise power and calibrated SNR equal to SNR2 under no jamming.

Observe that the BER experimental results with the calibrated SNR match reasonably with the theoretical results. In other words, each experiment result value is within ± 1 dB from the theoretical results. Observe also that the difference in SNR between the experimental and theoretical results becomes large and unstable when the SNR is low, e.g., smaller than 14 dB and 6 dB for 16PSK and QPSK, respectively. Different SNR values can be achieved by varying the

transmitting power gain with the “add noise” button turned off.

Note also that the maximum of the USRP 2932 TX power gain is limited to 30 dB. Hence, a very long-distance experiment is not feasible and unreliable due to the high free space path loss (which is inversely proportional to the square of the distance). This is why 83 cm was chosen to represent a long-distance experiment and 6 cm was chosen to represent a short-distance experiment.

If the distance between a TX and a RX is larger than a reference distance d_0 and smaller than the critical distance d_c , then a known free-space path loss model can be applicable for the

receiver power calculation. In other words, $P_r = P_t \left(\frac{\lambda \sqrt{G_t G_r}}{d} \right)^2$, where P_t , P_r , G_t , G_r , λ , and

d denote, respectively, transmit power, received power, transmit antenna gain, receive antenna gain, wavelength, and distance between the TX and RD. The reference distance d_0 can be computed as $d_0 = h_t$, where h_t is a transmit antenna height in a free space model. A critical

distance d_c is computed as $d_c = \frac{4h_t h_r}{\lambda}$ in a free-space model, where h_r is the receiver antenna

height. For example, if $h_t = 10$ m, $h_r = 3$ m, and $f_c = 2$ GHz for a microcell, then d_c is 800 m, whereas if $h_t = 3$ m, $h_r = 2$ m, and $f_c = 2$ GHz for an indoor cell, then d_c is 160 m. To use a free-space path loss model, the distance between a TX and a RX should be larger than d_0 . The free-space path loss model is sometimes difficult to apply in the lab because the TX and RX USRPs are connected to a common PC with cables, and the cable distances can be shorter than the reference distance d_0 , although the TX and RX USRPs are communicated in wireless.

Fig. A-4 shows the experimental results with the transmitter power gain as a parameter. Solid curves represent theoretical results, and circles and stars represent the experimental results. Compare the experimental results for 16PSK modulation of 15 dB transmitter power gain and long distance (i.e., stars on middle top side) with the experimental results of 23 dB transmitter power gain and the same long distance (i.e., circles on middle right side). The theoretical transmitter gain difference is 8 dB. Also observe that the calibrated SNR difference between the two experimental cases is about 7 dB, which is close to the theoretical difference of 8 dB.

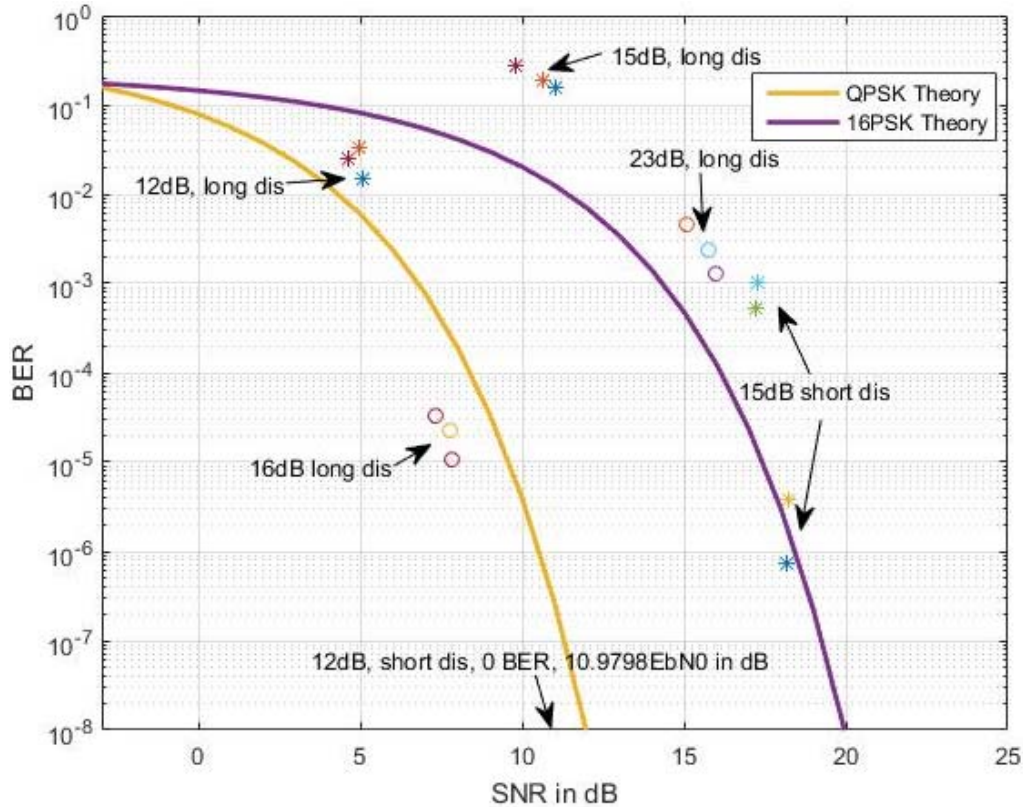


Fig. A-4. Experimental BER results with calibrated SNR and transmitter gain as a parameter.

Again, compare the experimental results for QPSK modulation of 12 dB transmitter power gain and long distance (i.e., stars on top left side) with the experimental results of 16 dB transmitter power gain and the same long distance (i.e., middle left side). As can be seen, the experimental results difference between the two cases is about 3.5 dB, which is close to the theoretical difference of 4 dB in the transmitting power gain for the two cases.

From the observed results in Figs. A-3 and A-4, the following can be stated:

1. A higher transmitter power gain causes a higher SNR and a lower experimental BER.
2. A longer distance shows a lower experimental receive power.
3. The experimental SNR difference is within 1 dB from the theoretical transmitter power gain difference.
4. Experimental results for both long and short distances are close to the corresponding theoretical results.
5. For the given set of parameters, 1 to 2 dB difference in SNR was observed at the same BER from one experiment to another. This is because the USRP is not a calibrated device.
6. Experimental results are not stable and reliable when the SNR < 6 dB for QPSK and the SNR < 14 dB for 16PSK.

Fig. A-5 demonstrates the experimental results with a jamming signal. The locations of a sender USRP, a receiver USRP, and a jammer USRP are located in a triangle shape with an equal side distance of 83 cm. A PC controls the sender and receiver USRP parameters, and another PC controls the jammer USRP parameters. Circles on the middle right side represent

experimental results for 16PSK without jamming, and stars on the top right side represent the case of jamming. Here, the jamming power gain is chosen to be equal to the sender power gain of 23 dB. But the jammer sends a different information package because the PN sequence order of the jammer is chosen differently from that of the sender. Observe that the BER is significantly degraded from 10^{-5} to 0.3, due to the jamming signal presence, and the calibrated SNR increases slightly, due to the jammer's power.

Also, the bottom arrow on the left represents the case without jamming signal for QPSK modulation, and bottom arrow on the right represents the case with jamming. Both cases use the same transmit power gain, which is equal to 23 dB, and the jamming signal uses the same transmit power gain of 23 dB. The BER is still zero even under jamming. This is because the SNR is too high, such as 18.26 dB for the QPSK, when the jamming signal is not present. However, if the transmitting power gain decreases from 23 to 13 dB under the same 23-dB jamming power condition, then the BER performance is degraded significantly from 0 to 0.3. Stars in the middle at the top represent this case.

Figs. A-6 and A-7 show experimental setups for the cases of short distance and long distance, respectively. Observe that two USRPs are controlled by one PC and collected by a switch. Fig. A-8 shows all experiment devices used here: three 2932 USRPs, one vector analyzer (Anritsu MS2026A), and an MXA signal analyzer (Agilent Technologies N9020A). A vector analyzer signal can behave as a jammer signal, and a signal analyzer can show the received power spectral density.

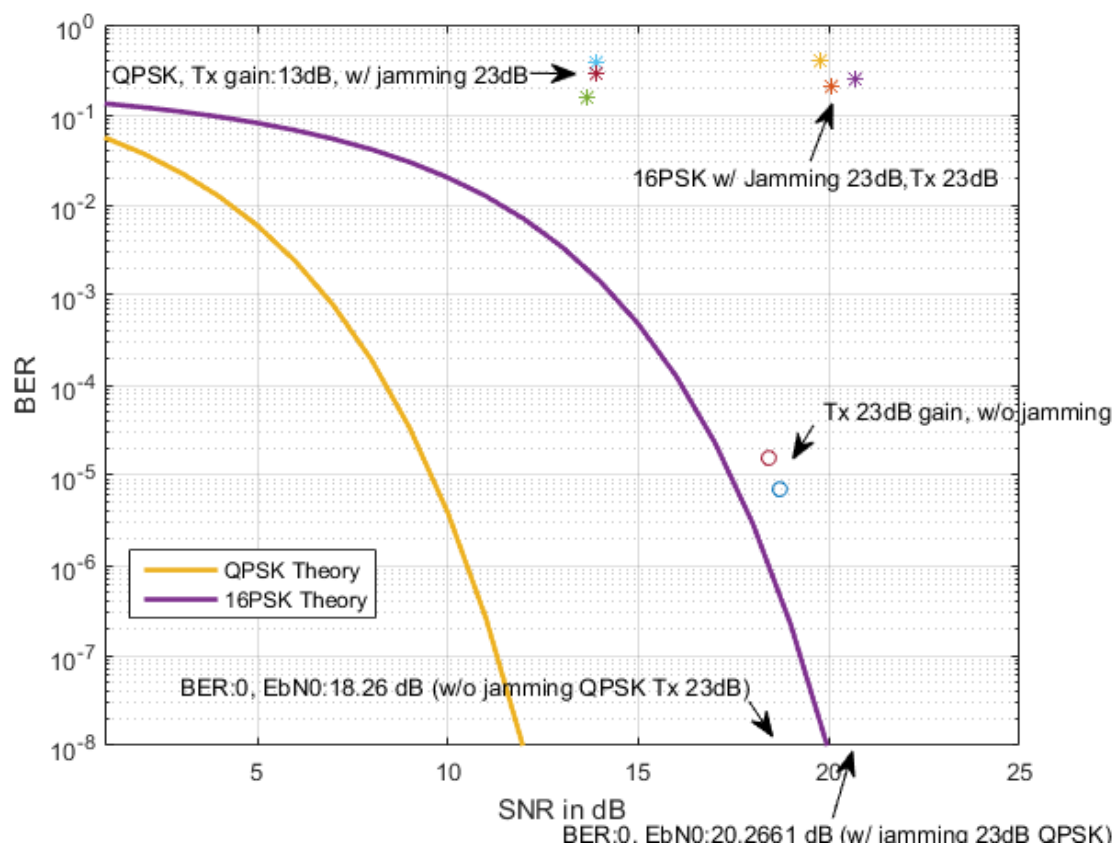


Fig. A-5. Experimental results with jamming.



Fig. A-6. Short-distance experiment setup.

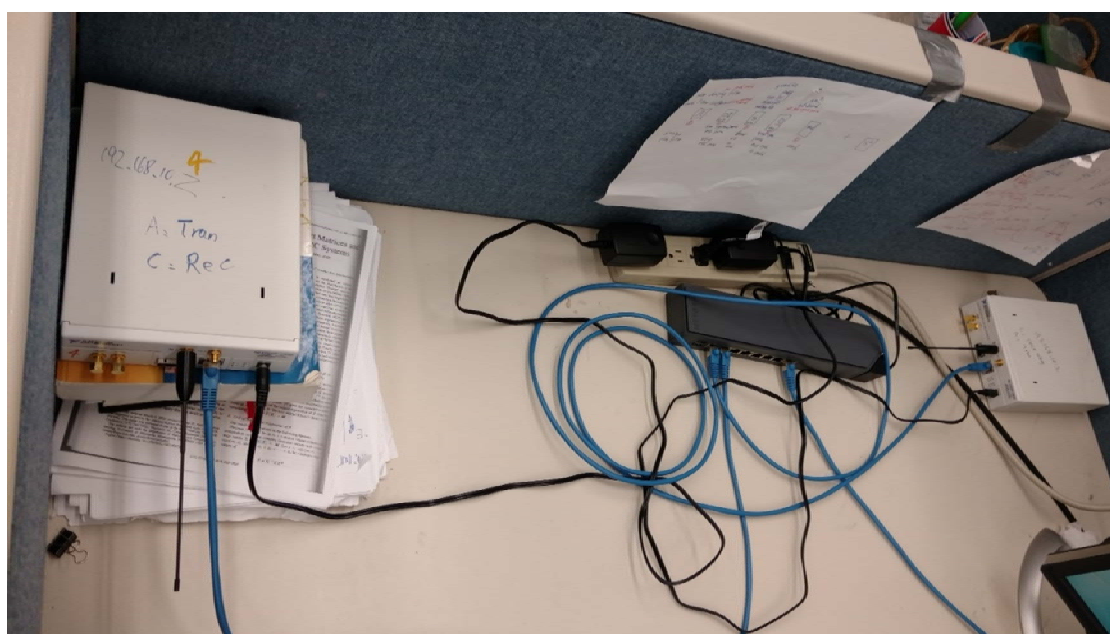


Fig. A-7. Long-distance experiment setup.

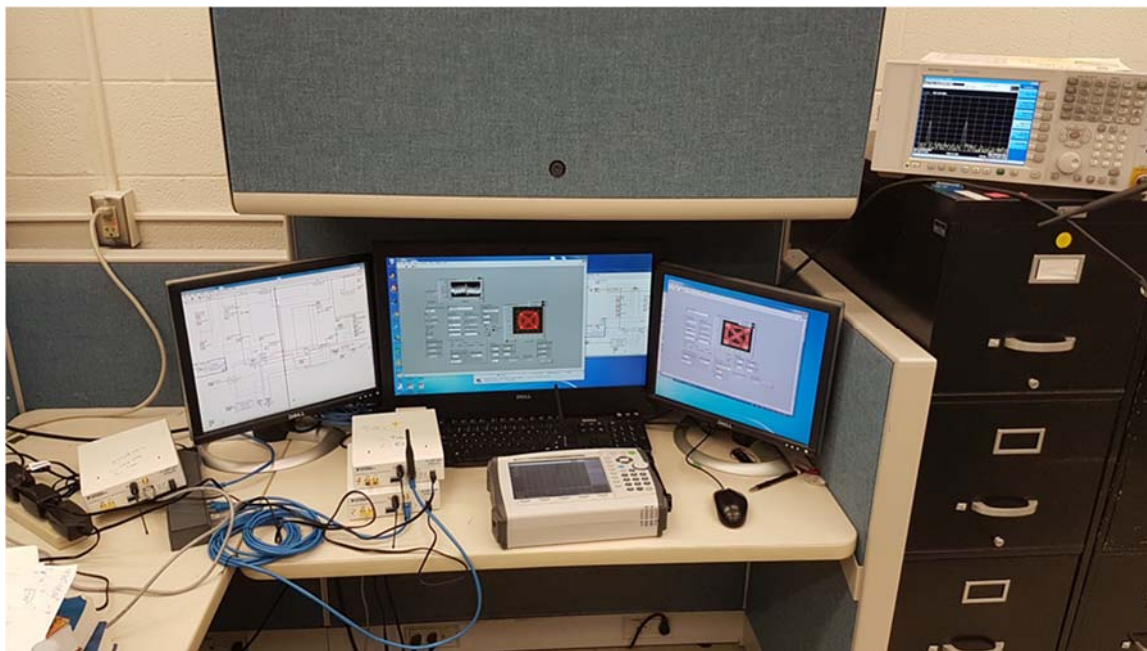


Fig. A-8 Experiment devices used.

Appendix B: USRP Back Panel Block Diagrams

APPENDIX B - LIST OF FIGURES

| | |
|--|----|
| Fig. B-1. Block diagram for State 1 “Initialize” at transmitter..... | 47 |
| Fig. B-2. Block diagram for State 2 “Configure Hardware” at transmitter..... | 49 |
| Fig. B-3. Block diagram for State 3 “Configure Signal” at transmitter..... | 51 |
| Fig. B-4. Block diagram of detail of Section 1 from Fig. B-3 (State 3 “Configure Signal”) at transmitter..... | 53 |
| Fig. B-5. Block diagram for State 4 “Generate Message” at transmitter..... | 55 |
| Fig. B-6. Block diagram for State 1 “Initialize” at receiver..... | 57 |
| Fig. B-7. Block diagram for State 3 “Configure Signal” at receiver..... | 59 |
| Fig. B-8. Block diagram for State 4 “Begin Receive” at receiver..... | 61 |
| Fig. B-9. Block diagram for State 5 “Calculate BER” at receiver..... | 63 |
| Fig. B-10. PSD when one USRP is turned on with 10 dB transmit power gain..... | 64 |
| Fig. B-11. PSD when two USRPs are turned on simultaneously on with same 10 dB transmit power gain and parameters..... | 65 |
| Fig. B-12. PSD when signal is transmitted from vector network analyzer..... | 65 |

Preface

Appendix B of this report describes block diagrams of the back panel of a Universal Software Radio Peripheral (USRP) hardware radio communications system, which was built for the research project “Optimum Boundaries of Signal-to-Noise Ratio for Adaptive Code Modulations,” U.S. Air Force Research Laboratory, Grant Award Number FA9453-16-1-0049. Three 2932 USRPs—one for a transmitter (TX), another for a receiver (RX), and the third for a jammer transmitter—were employed for the test from October 2016 to May 2017. It is expected that the observations and experiences in this report will be useful for other ongoing and future tests involving USRPs.

The transmitter virtual instrument (VI) has four states: State 1, “Initialize,” which is processed first and shown in Fig. B-1; then State 2, “Configure Hardware,” which is shown in Fig. B-2; then State 3, “Configure Signal,” which is shown in Fig. B-3; and finally State 4, “Generate Message,” which is shown in Fig. B-5. Fig. B-4 shows a block diagram of a detail of Section 1 from Fig. B-3 (State 3 “Configure Signal”) at transmitter.

Sections of the transmitter block diagrams in Appendix B are referred to by their **orange** numbers and are explained below.

Transmitter Block Diagram for State 1 “Initialize” Shown in Fig. B-1

Fig. B-1 is a block diagram for State 1 “Initialize” at the transmitter.

A combination of **Sections 1, 2, 3, and 4** in this block diagram is referred to as a state machine, which relies on user-input and/or in-state calculation and determines the next state. Section 1 is a feedback loop. **Sections 2 and 5** indicate the case structure. A user can insert different cases into the structure. A case structure behaves like a statement “switch” in C++. **Section 3** indicates what the initial state should be and is referred to as “Initialize” in Fig. B-1. **Section 4** shows what the next state should be after the current state and is referred to as “Configure Hardware” in Fig. B-1.

Section 5: This case structure stores a different type of M-ary phase shift keying (MPSK). The current modulation shown in Fig. B-1 is 16PSK.

Section 6: This VI opens a transmit session to the device user specified in the **device name** input and returns the **session handshake output**.

Section 7: This indicates that the session **handshake** will be closed. Note that this VI is on the outside of the feedback loop, meaning that the VI can be reached only after all the loop functions are finished. Only components on the inside of the case structure can be changed for different states.

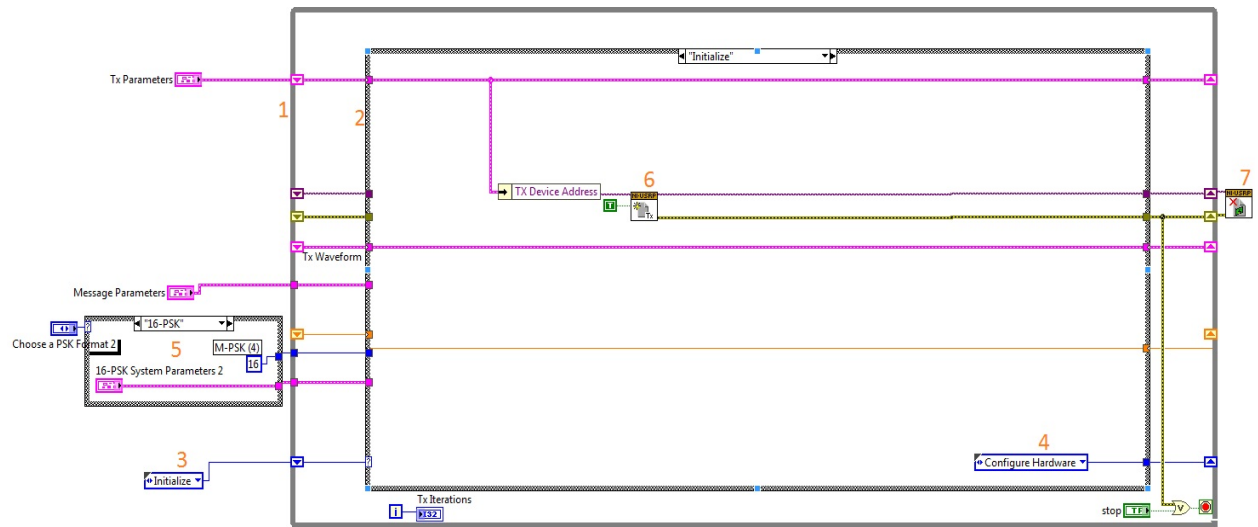


Fig. B-1. Block diagram for State 1 “Initialize” at transmitter.

Transmitter Block Diagram for State 2 “Configure Hardware” Shown in Fig. B-2

Section 1: This VI configures the properties of the TX or receiver (RX) signal. A user can define the properties as shown on the left side, and the VI will apply this information to the device. Note that an USRP is not a calibrated one. For example, the transmitter gain value does not represent the device output of the actual gain.

Sections 2 and 3: The normal and upside down triangles in these sections represent a pair of shift registers. For example, the data sent to the shift register marked as Section 2 will be fed back to the shift register marked as Section 3, then go to Section 2 and so on repeatedly until the loop stops.

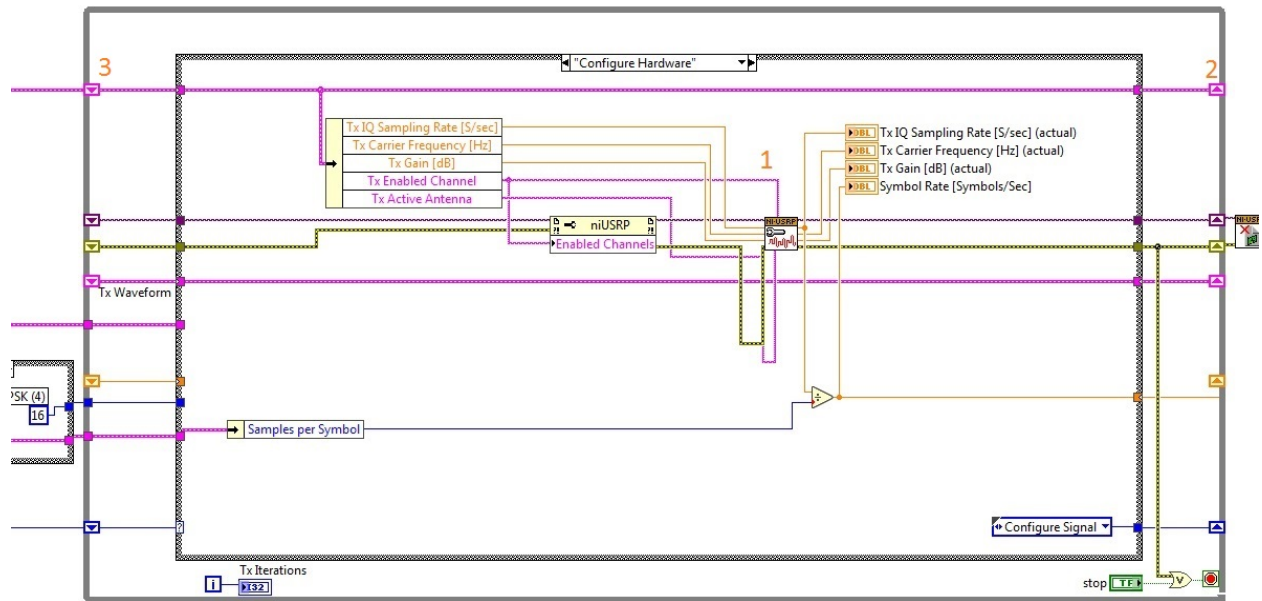


Fig. B-2. Block diagram for State 2 “Configure Hardware” at transmitter.

Transmitter Block Diagram for State 3 “Configure Signal” Shown in Fig. B-3

Section 1: This VI is a combination of modulation and synchronization (sync) bits, which generate and modulate a baseband PSK signal. Refer to Fig. B-4 for details of this section.

Section 2: In this case structure, if the condition is true, then an AWGN noise with a given power will be created from this VI. Note that this AWGN noise is not created by the USRP device but rather by the VI function. This function was built only for testing purposes. In the final experiment, this AWGN noise was not used at all, and the condition was always set to false.

Section 3: This VI shows a constellation plot.

Section 4: This blue thin wire means that only a single data stream is transmitted.

Section 5: This pink thick wire carries multiple stream information, e.g., device name, gain, sampling rate, and so on.

Note: Compare the thickness of the wires in Sections 4 and 5.

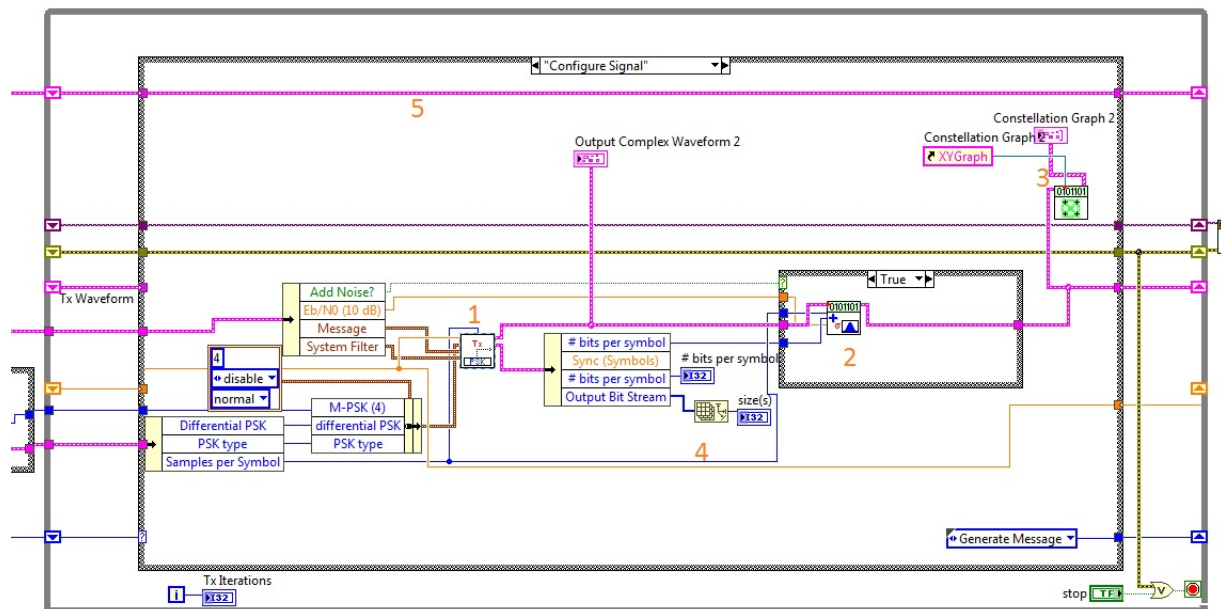


Fig. B-3. Block diagram for State 3 “Configure Signal” at transmitter.

Transmitter Block Diagram of Detail of Section 1 from Fig. B-3 Shown in Figure B-4

Section 1: The pulse shaping filter is designed based on the user setting, such as the type of filter, roll-off factor, and filter length.

Section 2: The PSK modulation parameters, such as a PSK type and M value, are prepared in this VI.

Section 3: This VI prepares the bit stream to modulate. The bit stream is composed of guard bits, sync bits, and information bits. All guard bits are set to 1. Information bits and sync bits are generated from a PN sequence. The default PN order for sync bits is 31, which is the highest possible order for a PN sequence generation at the VI. And it is not possible to change this order at a front panel due to confusion. However, the PN order for information bits generation can be modified at a front panel.

Section 4: This VI constructs an FSK, PSK, QAM, MSK, PAM, ASK, or CPM synchronization parameters cluster that the user can pass to a demodulation VI, using an array of either sync bits or sync numbers. In this case, the sync bits will be mapped into symbols, because the receiver looks for symbols, not bits.

Section 5: The bit stream is modulated into PSK symbols here.

Section 6: All types of different data are bundled into a thick pink wire referred to as “Signal Description.” This method is called “bundle by name.”

Section 7: This represents a logic OR gate.

Section 8: This represents a typical control. For example, the case in Section 8 is the control of a symbol rate in Hz.

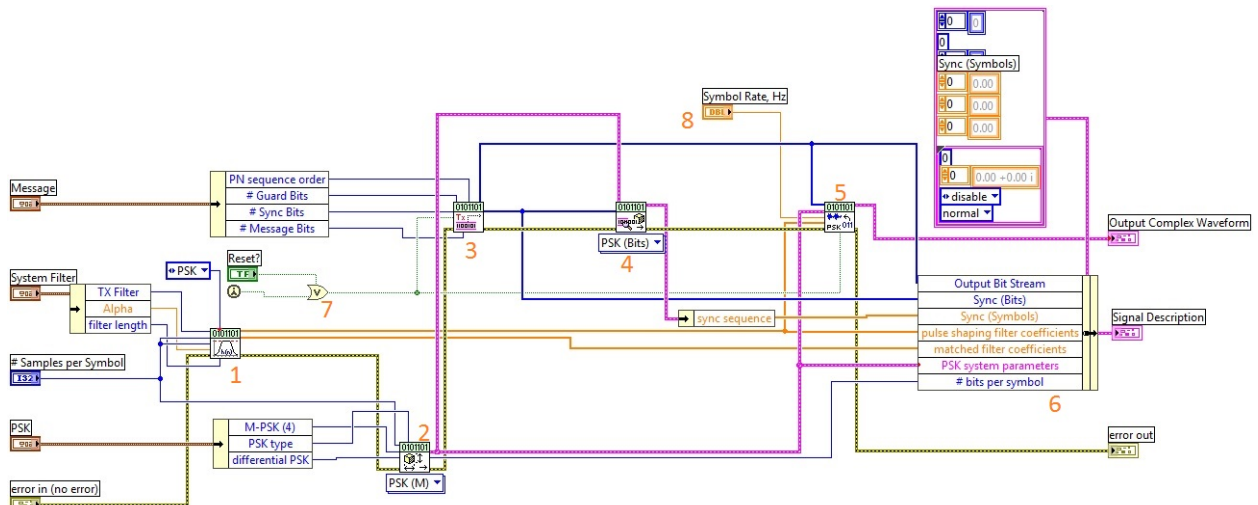


Fig. B-4. Block diagram of detail of Section 1 from Fig. B-3 (State 3 “Configure Signal”) at transmitter.

Transmitter Block Diagram for State 4 “Generate Message” Shown in Fig. B-5

Section 1: This VI controls for an USRP to transmit the data following all the previous preparation setups.

Section 2: First, this function unbundles the transmitting data from a bundled multiple wire data stream. Second, it finds out the size of transmitting data, and shows the size at a front panel.

Section 3: This is the next state “Generate Message.”

Section 4: This is the current state “Generate Message.”

Note: Since the next state in Section 3 is the same as the current state in Section 4, this implies that the “Generate Message” state will be processed repeatedly again and again. In other words, the same information will be sent to the air repeatedly.

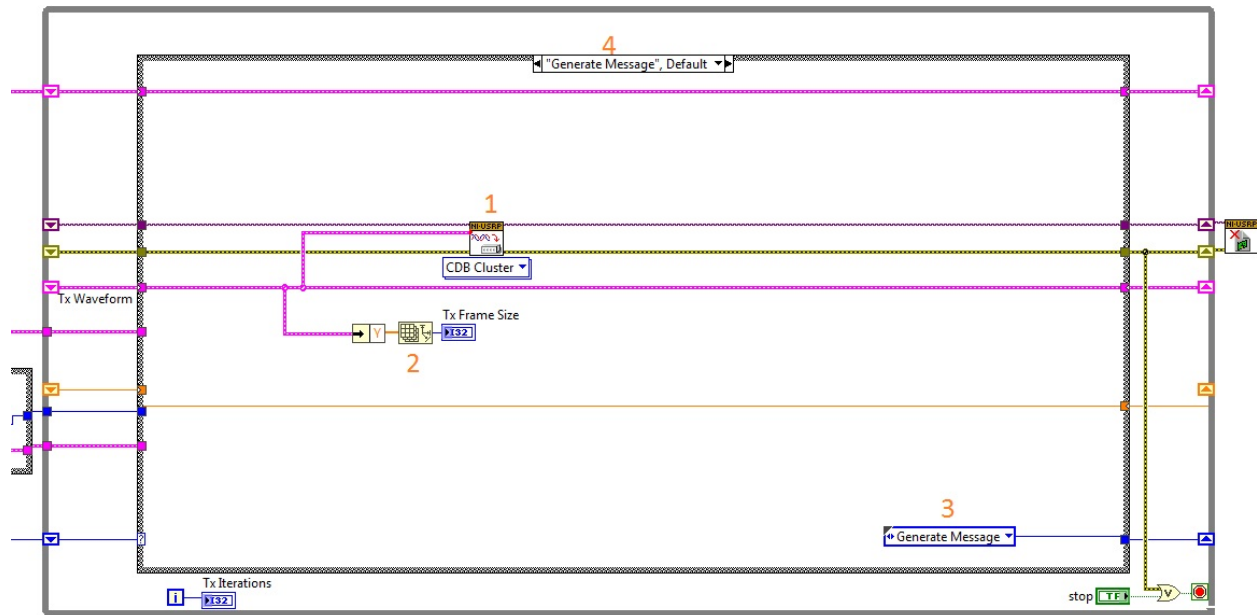


Fig. B-5. Block diagram for State 4 “Generate Message” at transmitter.

In the receiver virtual instrument, there are five states: State 1, “Initialize,” which is processed first and shown in Fig. B-6; then State 2, “Configure Hardware,” which is the same Tx block diagram shown in Fig. B-2; then State 3, “Configure Signal,” which is shown in Fig. B-7; then State 4, “Begin Receive,” which is shown in Fig. B-8, and finally State 5, “Calculate BER,” which is shown in Fig. B-9.

Sections of the receiver block diagrams in Appendix B are referred to by their **orange** numbers and are explained below.

Receiver Block Diagram for State 1 “Initialize” Shown in Fig. B-6

Fig. B-6 is a block diagram for State 1 “Initialize” at the receiver.

Section 1: This VI opens the receiving session to the RX USRP. This function is the same as for Section 6 shown in Fig. B-1, but for receiving.

Section 2: This is the current state “Initialize.”

Section 3: The main purpose of this section, located on the very right side, is to check whether the correct experimental outputs are being shown at the receiver front panel or not, e.g., the average BER and average SNR. Note that there are some hidden indicators. They are not for experiment output results but for simulation debugging and testing.

Notes:

1. This is a state machine again. Where there are four states in the transmitter VI, as shown previously in Figs. B-1, B-2, B-3, and B-5, there are five states for the receiver VI, as shown in Figs. B-6.
2. The case structure on the very left is for the receiver modulation selection, which is currently QPSK.
3. The box on the top right is a “for loop.”
4. The question mark node at the left of Section 3 is called a “conditional tunnel,” meaning that the tunnel output depends on the condition. If the condition is false, then there is no output.

Receiver Block Diagram for State 2 “Configure Hardware”

The next state in the Rx block diagram in Fig. B-6 is “Configure Hardware.” This structure is the same as the Tx block diagram, shown previously in Fig. B-2.

Receiver Block Diagram for State 3 “Configure Signal” Shown in Fig. B-7

The receiver function of Section 1 shown in Fig. B-7 is the same as the transmitter function of Section 1 in Fig. B-3. This function at the receiver prepares for the sync bit pattern, modulation parameters, filter pattern for demodulation, BER calculation, and SNR calculation in Section 2 shown in Fig. B-7.

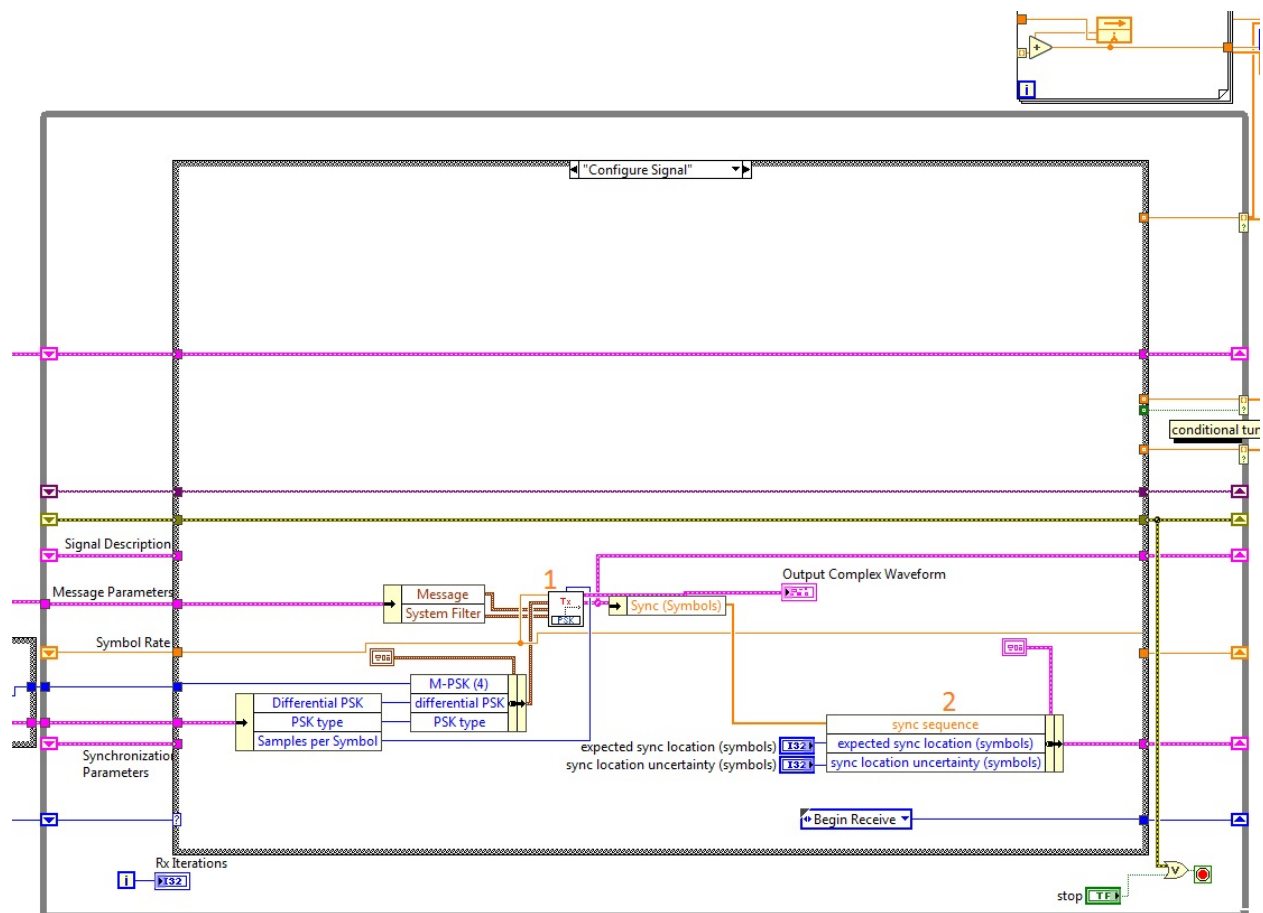


Fig. B-7. Block diagram for State 3 “Configure Signal” at receiver.

Receiver Block Diagram for State 4 “Begin Receive” Shown in Fig. B-8

Section 1: The USRP Initiate VI in Fig. B-8 starts the waveform acquisition in a receive session.

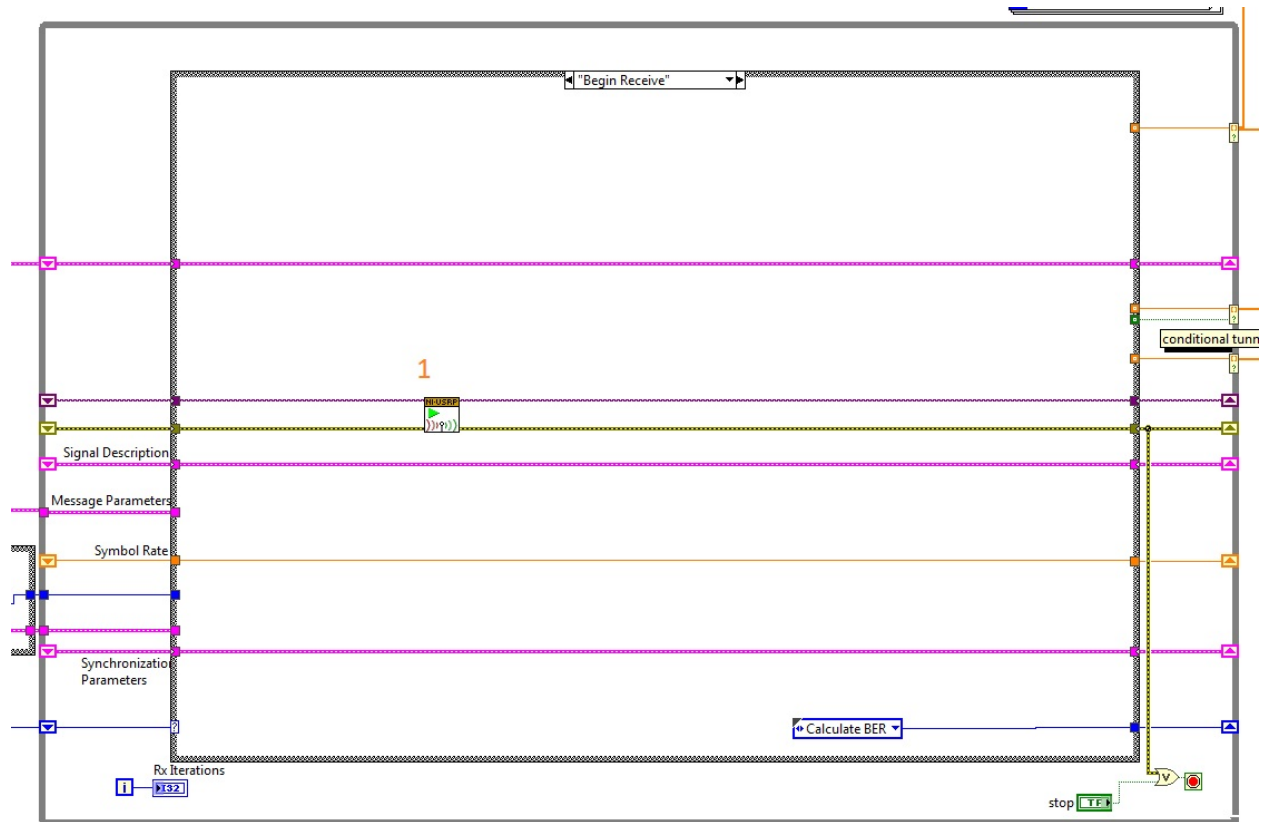


Fig. B-8. Block diagram for State 4 “Begin Receive” at receiver.

Receiver Block Diagram for State 5 “Calculate BER” Shown in Fig. B-9

Section 1: This VI lets the RX USRP fetch data from the specified channel list.

Section 2: The received information will be demodulated into the PSK baseband symbols using the defined parameters.

Section 3: This VI prepares the recovered signal for a constellation graph display.

Section 4: This VI also prepares the recovered signal for a constellation graph display.

Section 5: This VI is for testing and debugging in the SNR calculation. The outputs are hidden at the Rx front panel.

Section 6: BER is calculated based on the reference pattern and BER trigger threshold.

Section 7: The signal power and AWGN power are estimated. However, the noise power estimate is incorrect because it is proportional to the transmitter power gain; hence, the SNR is constant regardless of the transmitter power gain. This report does not use the AWGN power estimation in this section. The correct noise power estimation is presented in the RX front panel discussion in Appendix A of this report.

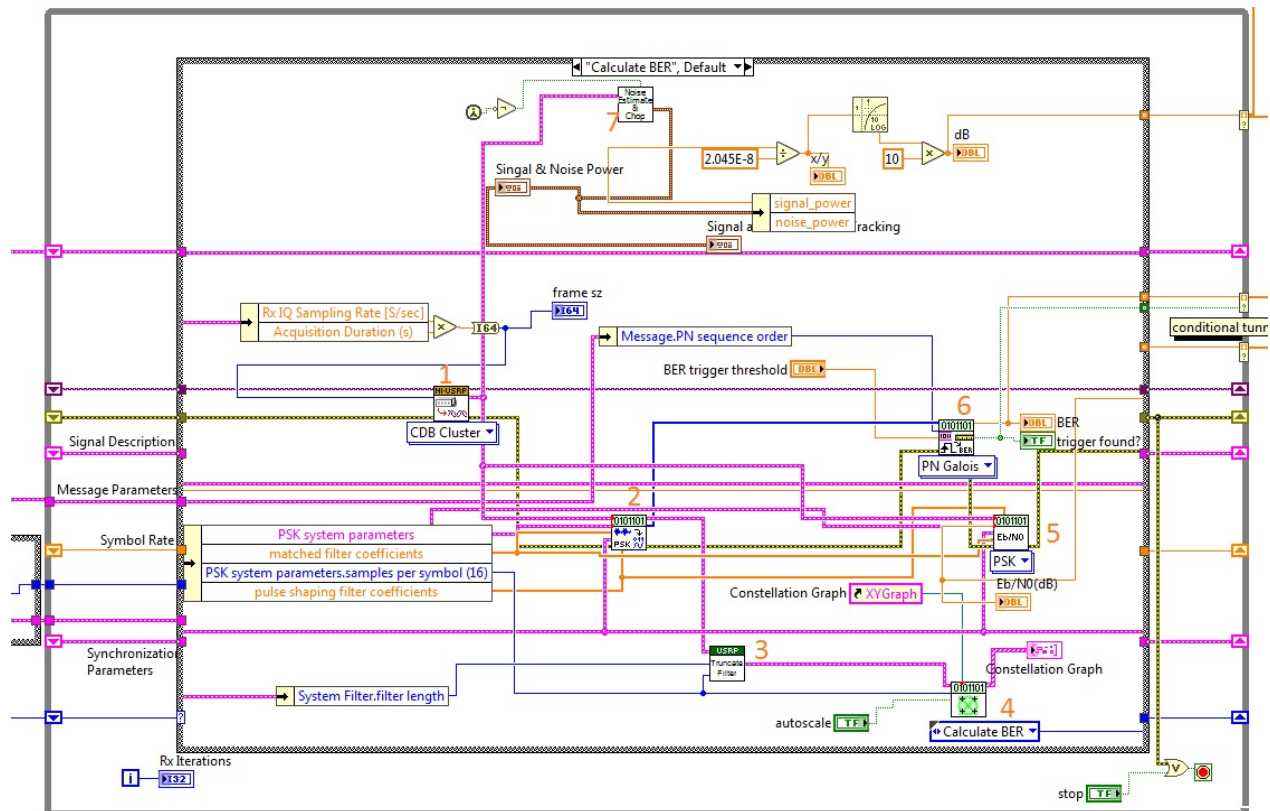


Fig. B-9. Block diagram for State 5 “Calculate BER” at receiver.

Maximum Signal Analyzer and Vector Network Analyzer

Fig. B-10 shows the power spectral density (PSD) plotted by an Agilent MAXA signal analyzer with -20 dBm reference level when one USRP 2932 is turned on with 10 dB transmit power gain. Observe in Fig. B-11 that the peak height of the summed signal PSD increases when the second USRP 2932 is simultaneously turned on with the same 10 dB power gain and the same parameters as in the first USRP. The distance between the two USRPs and the signal analyzer was about 0.8 m. Observe that Figs. B-10 and B-11 show very unstable PSD peaks in time. However, it can be seen in Fig. B-12 that the PSD peak becomes stable when a vector network analyzer instead of a USRP transmits a signal. This teaches us a lesson that the noise power in an USRP is not calibrated and causes instability, but the signal from a vector analyzer is well calibrated and stable.

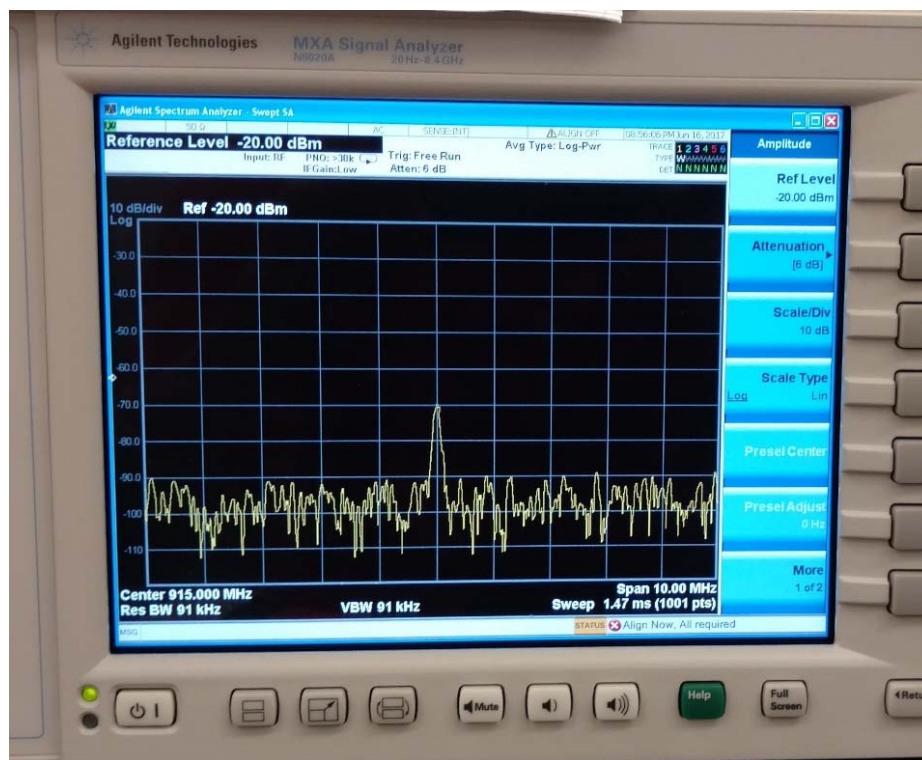


Fig. B-10. PSD when one USRP is turned on with 10 dB transmit power gain.

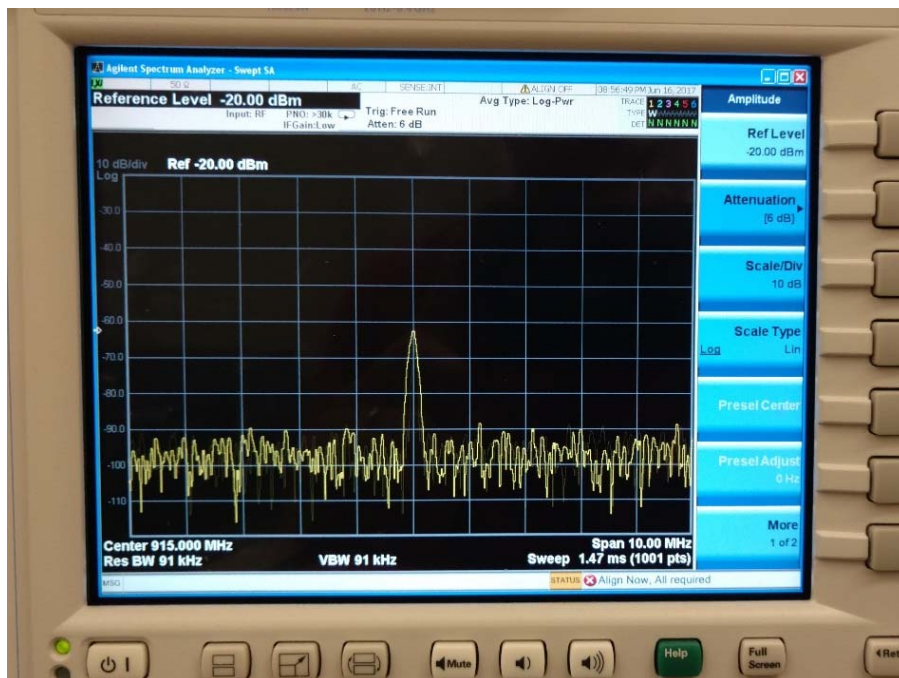


Fig. B-11. PSD when two USRPs are turned on simultaneously on with same 10 dB transmit power gain and parameters.

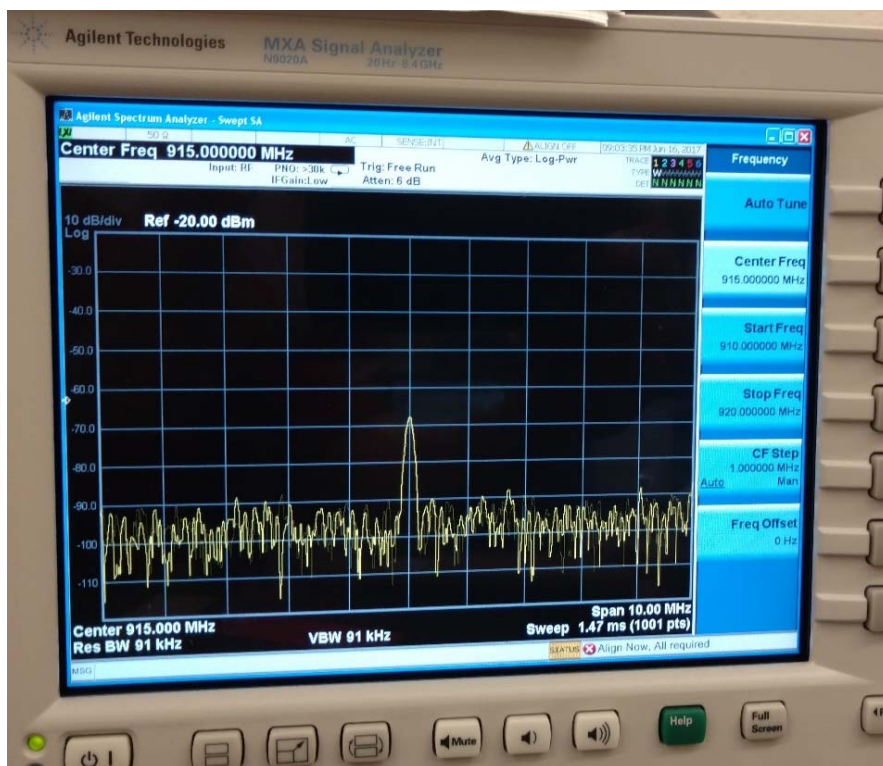


Fig. B-12. PSD when signal is transmitted from vector network analyzer.

List of Acronyms and Abbreviations

| | |
|-------------|---|
| ACM: | adaptive code modulation |
| AFRL: | Air Force Research Laboratory |
| AWGN: | additive white Gaussian noise |
| BER: | bit error rate |
| β : | partial-band noise jamming fraction |
| dB: | decibel |
| DVB: | digital video broadcasting |
| DVB-RCS: | digital video broadcasting-return channel via satellite |
| DVB-S2: | second-generation digital video broadcasting satellite |
| DTN: | disruption/delay tolerant network |
| 8PSK: | 8-ary phase-shift keying |
| E_b/N_0 : | bit-energy-to-noise power spectral density ratio |
| E_s/N_0 : | symbol-energy-to-noise power spectral density ratio |
| E_b/N_J : | bit-energy-to-jamming power spectral density ratio |
| E_s/N_J : | symbol-energy-to-jamming power spectral density ratio |
| FEC: | forward error correction code |
| IP: | internet protocol |
| JSI : | jamming state information |
| K : | Rician fading factor |
| LDPC: | low-density parity check code |
| LOS: | line-of-sight |
| MILSACOM: | military satellite communications |
| MPSK: | M-ary phase-shift keying |
| NLOS: | non-line-of-sight |
| PBNJ: | partial-band noise jamming |
| PC: | personal computer |
| QPSK: | quadrature-phase-shift keying |
| RX: | receiver |
| SJNR: | symbol energy-to-jamming-plus-noise ratio |
| SNR: | signal-to-noise ratio |
| TX: | transmitter |
| USRP: | universal software radio peripheral |

DISTRIBUTION LIST

| | |
|-------------------------------------|-------|
| DTIC/OCF | |
| 8725 John J. Kingman Rd, Suite 0944 | |
| Ft Belvoir, VA 22060-6218 | 1 cy |
| AFRL/RVIL | |
| Kirtland AFB, NM 87117-5776 | 2 cys |
| Official Record Copy | |
| AFRL/RVSW/Khanh Pham | 1 cy |

(This page intentionally left blank)